

Stray-radiation correction as applied to the Leiden/Dwingeloo survey of HI in the Galaxy

Dap Hartmann^{1,2}, P.M.W. Kalberla³, W.B. Burton¹ and U. Mebold³

¹ Sterrewacht Leiden, Postbus 9513, 2300 RA, Leiden, The Netherlands

² Harvard-Smithsonian Center for Astrophysics, 60 Garden Street, Cambridge, MA 02138, U.S.A.

³ Radioastronomisches Institut der Universität Bonn, Auf dem Hugel 71, 53121 Bonn, Germany

Received November 27, 1995; accepted February 6, 1996

Abstract. — This article describes the stray-radiation correction that was applied to the HI observations of the Leiden/Dwingeloo survey of Hartmann & Burton. This correction involved convolving the empirically-determined antenna pattern with the measured all-sky HI distribution. The importance of the correction is demonstrated and practice regarding its application described. The general algorithm used here is presented. The results obtained with this algorithm are compared to those following from other methods. The 0.07 K sensitivity level of the survey depends critically on the success of the stray-radiation correction.

Key words: methods: data analysis — surveys — radio lines: ISM — telescopes

1. Introduction

The Leiden/Dwingeloo survey of neutral atomic hydrogen in our Galaxy comprises observations of the entire sky north of $\delta = -30^\circ$. It represents an improvement over earlier large-scale HI surveys by an order of magnitude or more in at least one of the principal parameters of sensitivity, spatial coverage, or spectral resolution. The publication by Hartmann & Burton (1996) includes a description of the observational procedures, an atlas of representative slices through the (l, b, v) data cube, and a CD-ROM containing the data themselves; additional details of the observing and reduction procedures are given by Hartmann (1994). The Hartmann & Burton survey is intended as a resource amenable to a wide range of investigations of the galactic interstellar medium.

The angular resolution of the survey was set by the 36' beam width of the Dwingeloo 25-m telescope. The observations were made on a grid with a true-angle lattice spacing of 0.5 in both l and b . The spectral resolution was set by the spacing of 1.03 km s⁻¹ between each of the 1024 channels of the DAS digital autocorrelation spectrometer; the kinematic range of the material covers velocities (measured with respect to the Local Standard of Rest) between -450 km s⁻¹ and +400 km s⁻¹. The characteristic rms limit on the measured brightness-temperature intensities is 0.07 K. Achieving this sensitivity level required that the data be corrected for contamination by stray radia-

tion; such contamination can contribute as much signal as would be measured by a perfect radio antenna. The Leiden/Dwingeloo is the first major HI survey to be corrected for contamination by stray radiation. (The sensitivity level of the earlier Hat Creek surveys did not warrant the correction; the influence of stray radiation in the Bell Labs data was only minor because the horn reflector is not blocked by a feed-support structure.) This article describes this crucial correction.

An ideal radio telescope would receive only radiation which is incident on the antenna from the direction in which the telescope is pointing; that radiation would be undisturbed by the antenna feed. A parabolic reflector like that in Dwingeloo, with the aperture partially blocked by the feed and its support structure, is certainly not perfect in this respect. Radiation may be received directly into the feed, and also scattered off the feed support legs; these legs also cast shadows on part of the antenna pattern. Using modern receivers, the sensitivity of the antenna in every direction allows the ubiquitously-distributed HI radiation to be received from every direction on the sky.

The Dwingeloo telescope is, of course, a blocked-aperture parabola of early design; at the sensitivity levels afforded by the modern electronics with which the telescope was equipped for the Hartmann & Burton survey, the effects of stray radiation are, as we demonstrate in this article, severe.

In this introductory section we first review the relevant characteristics of a telescope antenna. The

conventions used by Kraus (1966) and Rohlfs (1986) are adapted to the terminology of Kalberla (1978). The early recognition of stray radiation in HI observations is the subject of Sect. 1.2, followed in Sect. 1.3 by a summary of the various solutions which have been applied to this problem in the past.

1.1. Antenna pattern, main beam, and side lobes

The response of the aerial as a function of direction is known as the antenna pattern. Choosing θ and ϕ as the spherical antenna coordinates, where $\theta = 0^\circ$ represents the main-lobe pointing axis of the telescope, the normalized antenna pattern may be expressed as

$$P_n(\theta, \phi) = \frac{P(\theta, \phi)}{P_{\max}(\theta, \phi)}. \quad (1)$$

The beam solid angle Ω_a of the antenna, namely

$$\Omega_a = \int_{4\pi} P_n(\theta, \phi) d\Omega, \quad (2)$$

represents the equivalent solid angle in which all the power over $4\pi \text{ rad}^2$ is received by an ideal antenna. The sensitivity of that ideal antenna is defined as $P_n \equiv 1$ over Ω_a , and $P_n \equiv 0$ for all other directions. Such a theoretical telescope antenna would thus receive all its radiation from the beam solid angle centered on the pointing direction of the telescope. For most real radio telescopes, the sensitivity is not confined to this pencil beam, but spread out over the full $4\pi \text{ rad}^2$. Most power is received in the telescope main beam, the extent of which is usually defined in terms of the *half-power beam width* (HPBW), i.e., the angle between the points where the power pattern of the antenna reaches half its maximum value. An alternative definition of the main-beam extent, and the one we use here, is the *beam width between first nulls* (BWFN). The main-beam solid angle Ω_{MB} is then defined as

$$\Omega_{\text{MB}} = \int_{\text{MB}} P_n(\theta, \phi) d\Omega. \quad (3)$$

A measure for the concentration of the power pattern in the main beam is given by the main beam efficiency, η_{MB} , where

$$\eta_{\text{MB}} = \frac{\Omega_{\text{MB}}}{\Omega_a}. \quad (4)$$

All directions outside the main beam are referred to as the *side lobes* or *stray pattern*, and the corresponding stray-pattern solid angle Ω_{SP} is

$$\Omega_{\text{SP}} = \Omega_a - \Omega_{\text{MB}}. \quad (5)$$

The ratio

$$\eta_{\text{SP}} = \frac{\Omega_{\text{SP}}}{\Omega_a} \quad (6)$$

is called the *stray factor*. Obviously, $\eta_{\text{MB}} + \eta_{\text{SP}} = 1$.

1.2. Early recognition of stray radiation

Even though most radio telescopes are primarily sensitive in the main beam, it is clear that radiation will also be received by the side lobes of the antenna pattern. This effect will be most pronounced for observations of ubiquitous radiation, such as galactic neutral hydrogen, because half of the stray pattern is directed towards the sky. Although the stray pattern is very much less sensitive than the main beam, the total contribution from the $2\pi \text{ rad}^2$ solid angle can be considerable. The problem is greatly reduced, although not eliminated, for horn antennas which have an aperture unblocked by the receiver or its feed, or by the support structure. Parabolic telescopes following new designs, such as that of the 100-m Green Bank Telescope currently under construction by the National Radio Astronomy Observatory, involve off-axis placement of the receiver system and thus a largely unblocked aperture; such telescopes will experience significantly reduced stray radiation effects.

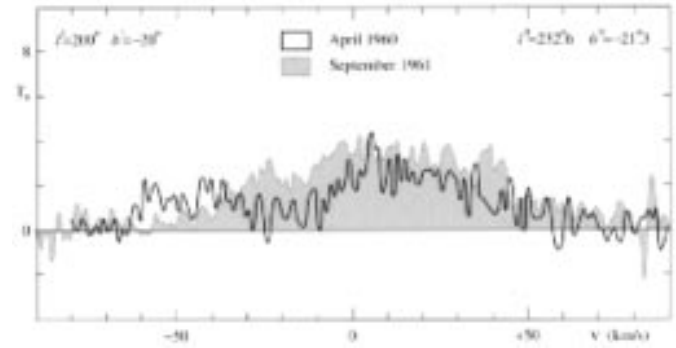


Fig. 1. First published detection of HI stray radiation (Van Woerden et al. 1962). Two spectra at $(l, b) = (200^\circ, -20^\circ)$ are plotted which were observed at different epochs, 17 months apart. Although the peak temperatures coincide, differences up to two units can be seen. The discrepancies were correctly interpreted as radiation received in the side lobes of the antenna pattern. The orientation of the brightest parts of the sky as well as the placement of the most sensitive areas in the stray pattern are different for the different epochs, as is the LSR velocity correction corresponding to the differing telescope pointings

Van Woerden (1962) was the first observer to interpret variations in HI spectra as due to stray radiation. After carefully reducing spectra observed in Dwingeloo during different seasons, he concluded that the profiles were contaminated by emission that was received outside the main beam of the antenna. He coined the term *stray profile* for this spectral emission contribution. Figure 1 shows data originally published by Van Woerden et al. (1962). Two spectra are plotted of a position in Orion that was observed at two different epochs, 17 months apart. Although the spectral noise is quite large (~ 0.5 units), significant differences between the spectra are seen. The peak temperatures are equal, but discrepancies of up to 2 units are

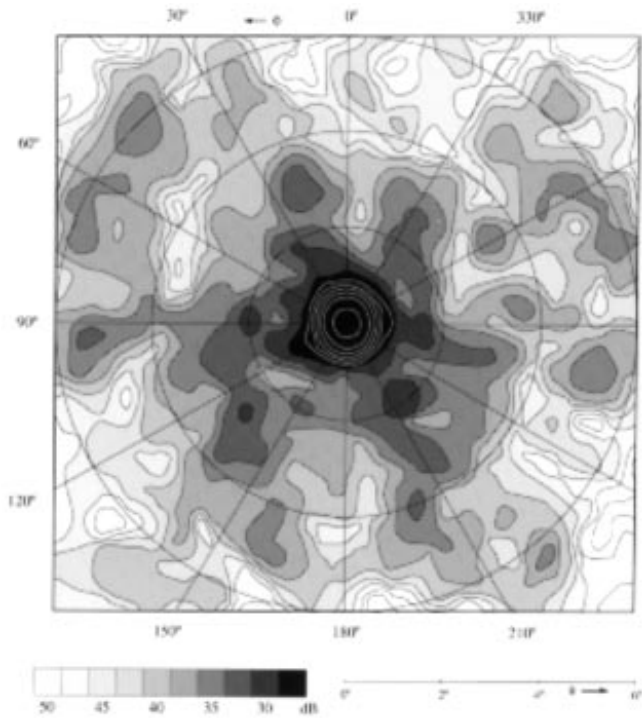


Fig. 2. Main-beam and near-sidelobe response of the Dwingeloo 25-m antenna pattern, measured by HBDG. The contours are in dB below the main beam intensity level. The main beam, to a level of -20 dB (the third-highest contour) is slightly elliptical, and measures $0^{\circ}.57 \times 0^{\circ}.62$ (HPBW). Note, in comparing these data to those shown in Figs. 3 and 4, that the angular distance from the main-beam axis, θ , extends only to 6° . These data did not suitably describe the NSL response of the Dwingeloo telescope during the 4-year observing period of the Hartmann & Burton survey

present elsewhere. When these data were taken, computers were hardly available, and it was impossible to treat the problem of stray radiation in a general way. Nevertheless, Van Woerden applied analytical methods to get a crude estimate of the side-lobe contamination. He assumed that $\eta_{\text{SP}} = 0.25$, and that it consisted of two equal contributions, namely, η_{ISO} and η_{SPILL} , where $\eta_{\text{SP}} = \eta_{\text{ISO}} + \eta_{\text{SPILL}}$ and $\eta_{\text{ISO}} = \eta_{\text{SPILL}} = 0.125$. The η_{ISO} was an isotropic component over the entire stray pattern, and η_{SPILL} represented the spillover ring, the region of the antenna pattern where radiation could enter the feed directly, i.e. without reflecting off the telescope dish. An estimate of the sky brightness was obtained, mainly from the first galactic-plane HI survey, observed with the Kootwijk telescope by Muller & Westerhout (1957). The isotropic component was approximated by a $\text{csc}(b)$ law. A model of the spillover ring was deduced from the geometry of the telescope, and estimated to lie in the range $120^{\circ} \leq \theta \leq 125^{\circ}$. Van Woerden then manually calculated stray-radiation contributions, by numerical integration of the stray pattern and the sky emission at the time of observing. Although his

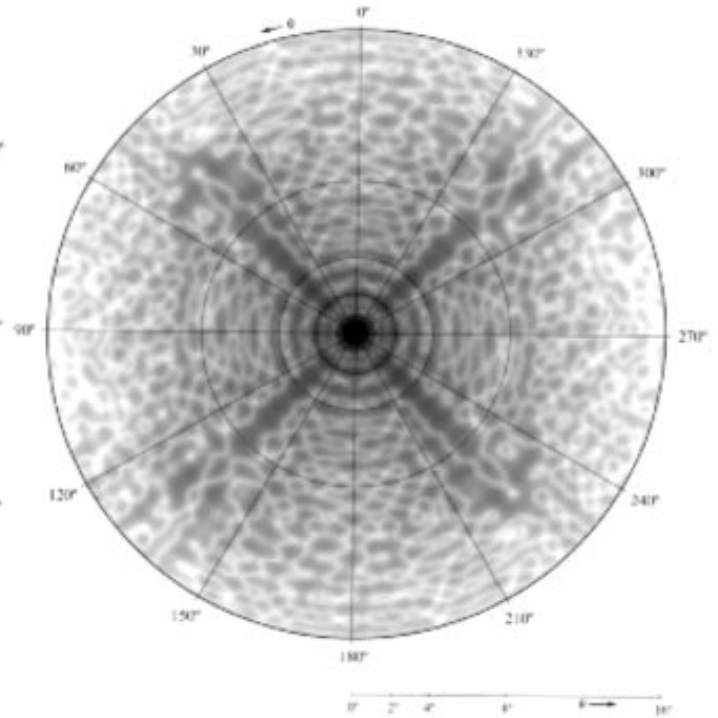


Fig. 3. Mean WSRT NSL pattern, generated from holographic measurements of 12 telescopes (Van Someren Greve 1991) and used as an approximation for the NSL pattern ($0^{\circ}.9 \leq \theta \leq 16^{\circ}$) of the Dwingeloo 25-m dish. The image is logarithmically scaled between -70 dB and -20 dB, relative to the main beam sensitivity. Concentric diffraction lobes are visible at $\theta = 2^{\circ}$, 3° , and 4° . Radiation scattered off the four feed-support legs causes regions of higher sensitivity, centered on $\phi = 45^{\circ}$, at 90° intervals

model calculations successfully explained the observed discrepancies in profiles of different epochs, no correction to the data was actually applied.

1.3. Further studies of stray radiation

After the existence of stray radiation had been empirically established, it was largely ignored for the next decade. The profiles published by Van Woerden (1962) and by Van Woerden et al. (1962) were all observed at galactic latitudes $|b| < 30^{\circ}$. Despite the high noise levels pertaining in the early 1960s, stray radiation had been clearly detected. Van Woerden also pointed out that the contamination by stray radiation would be relatively more pronounced in spectra observed at higher latitudes, where the HI content of the spectra would be much less, and where the spillover ring might intersect the galactic plane. Subsequent observations made with the Dwingeloo telescope were corrected using the simple model developed by Van Woerden. Although the model had not yet been confirmed by direct measurements at 1420 MHz, a 43-dB spillover ring had been found at 408 MHz. Raimond (1964) was the first to

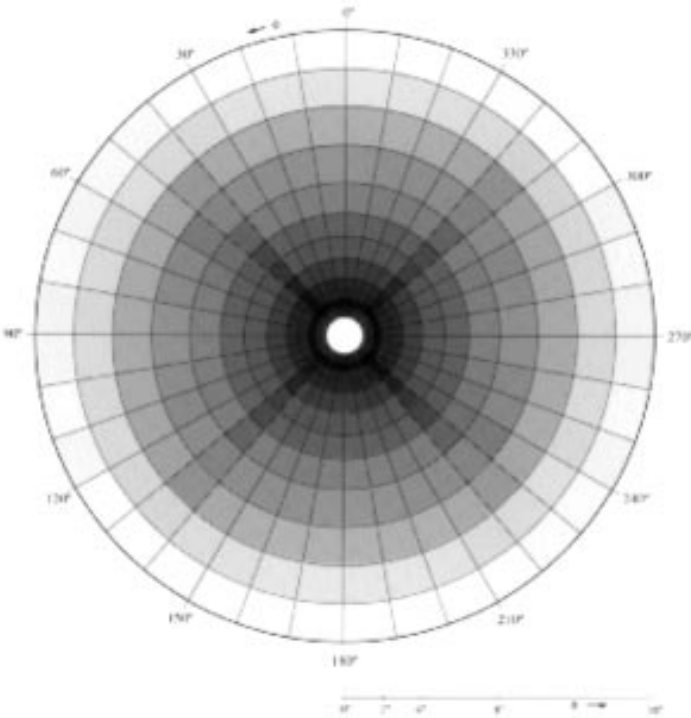


Fig. 4. Model of the NSL pattern ($0.9^\circ \leq \theta \leq 16^\circ$) of the Dwingeloo telescope, derived from the observed mean WSRT pattern shown in Fig. 3. The 468 cells which represent the kernel function of Eq. (14) are the elements for which the computer implementation is carried out. The image is logarithmically scaled. The concentric diffraction lobes (at main-beam distances $\theta = 2^\circ$, 3° , and 4°), and the enhanced stray regions caused by the feed-support legs (at antenna azimuth $\phi = 45^\circ$ modulo 90°), can be identified

use a computer to apply the correction. On a primitive early computer at the University of Leiden, he calculated the stray profiles for more than 500 spectra observed in a region surrounding two stellar associations in Monoceros.

After the sensitivity of HI receivers was greatly improved in the early 1970s, the importance of stray radiation was recognized anew. Mebold and Hachenberg had noticed discrepancies between repeated observations at high galactic latitudes made with the Effelsberg 100-m telescope. Their findings motivated Kalberla (1978) to address the problem of stray radiation in a generalized way and to develop a correction procedure. The availability of the Hat Creek HI surveys (Weaver & Williams 1973; Heiles & Habing 1974), which gave the first complete coverage of the northern sky, fulfilled one of the two requirements for accurately calculating stray profiles, namely an input HI sky. The second requirement was a detailed model of the antenna pattern which would sample this sky. Kalberla measured the antenna pattern of the 100-m Effelsberg telescope (HPBW = $9'$) to a radius of 2° from the main beam axis, and created an empirical model of the far sidelobes. For this model, he inspected

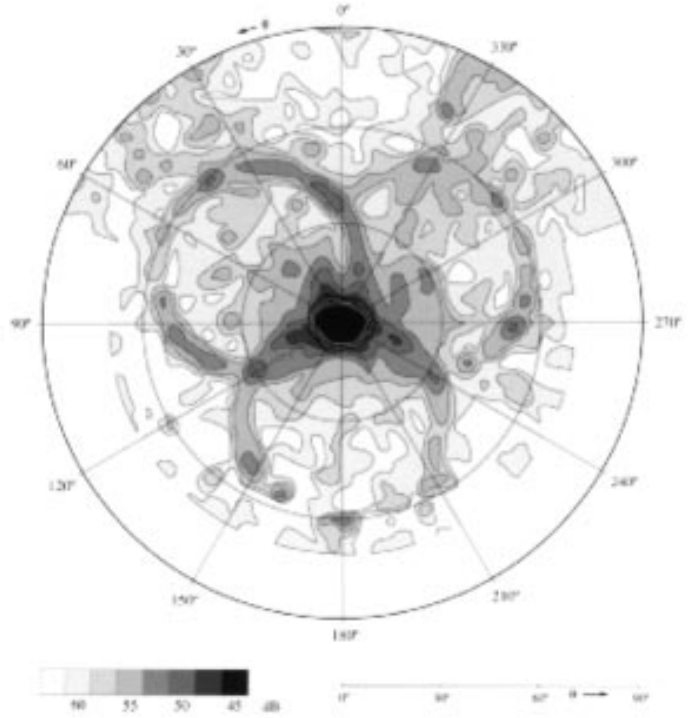


Fig. 5. Forward half ($0^\circ \leq \theta \leq 90^\circ$) of the antenna pattern of the Dwingeloo telescope, corresponding to the situation in 1968 (HBDG). Radiation scattered off the three feed-support legs causes the clearly visible stray cones of enhanced sensitivity, centered on $\theta = 30^\circ$. Regions of lower sensitivity are found in the directions where the support legs block (“shadow”) the feed at $\phi = 0^\circ$, 120° , and 240°

the characteristics of the Dwingeloo 25-m antenna pattern which had been extensively measured by Hartsuijker et al. (1972, hereafter HBDG). Prominent features in this stray pattern could be explained in terms of various structural components of the telescope (see also Sect. 3.4). This enabled Kalberla to predict the behavior of similar structures for the Effelsberg dish, and to create a model, albeit one with many free parameters. Repeated observations at different hour angles and at various epochs provided the material necessary to determine the relative sensitivities of the various components of the model. The empirically-tuned model consisted of a spillover ring, four stray cones (from radiation scattered off the feed support legs), and blockage (“shadowing”) of the pattern by the support legs. Additionally, four small components were found that were caused by reflections off the roof of the apex cabin. Hunt & Wright (1992) similarly discuss the stray-radiation correction necessitated by the geometry of the three-legged feed support of the Parkes 64-m telescope.

Kalberla’s work proved that stray-radiation corrections can be calculated from the antenna pattern and the sky brightness distribution. He showed that although an iterative correction procedure could be used, a more

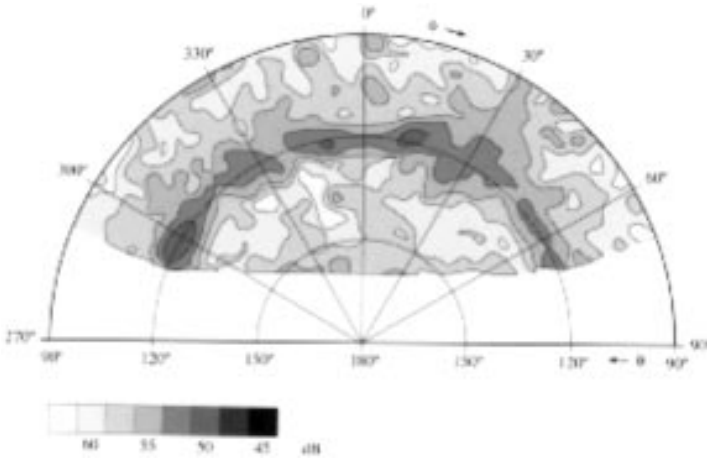


Fig. 6. Rear half ($90^\circ \leq \theta \leq 180^\circ$) of the antenna pattern of the Dwingeloo telescope corresponding to the situation in 1968 (HBDG). The same range in ϕ is mapped here as in Fig. 5. The most prominent feature is the spillover ring, centered at $\theta = 120^\circ$, which is about 5 dB more sensitive than the surrounding average; this structure accounts for 4.5% of the total sensitivity of the antenna pattern (see Table 1). (The data in Figs. 5 and 6 were determined using the 25-m antenna in tandem with a 7.5-m Würzburg dish. Such interferometric measurements were no longer feasible during the Hartmann & Burton survey)

direct solution existed. More details of the Kalberla Stray-Radiation Correction Algorithm (hereafter KSCA) are given in Sect. 2.1.

After applying the newly-developed correction procedure to the Effelsberg spectra, the inaccuracies in the brightness temperature scaling of corrected spectra became of the order of 10–20%. This should be compared to the inaccuracies of high-latitude spectra without stray-radiation correction; not uncommonly the stray-radiation component contains as much emission as the corrected signal. This stray-radiation correction algorithm has since become the standard correction applied for all galactic HI spectra measured with the Effelsberg telescope.

The effects of stray radiation are greatly reduced for observations made with a horn reflector. That realization motivated a major sky survey ($\delta \geq -40^\circ$) of galactic HI using the 20-ft horn-reflector (HPBW = 2°) at AT&T Bell Laboratories in Crawford Hill (Stark et al. 1992). The main beam efficiency of the Bell Labs telescope is very high ($\eta_{\text{MB}} = 0.92$), and most of the remaining sensitivity is in nearby sidelobes. A study of the far-sidelobe contamination of the published survey data was made by Kuntz & Danly (1992). They showed that the two known far sidelobes of the telescope (one at $\theta = 18^\circ$, probably caused either by the drive wheel or by the weather cover of the horn; the other at $\theta = 70^\circ$, probably caused by diffraction from the edge of the reflector) caused stray radiation that

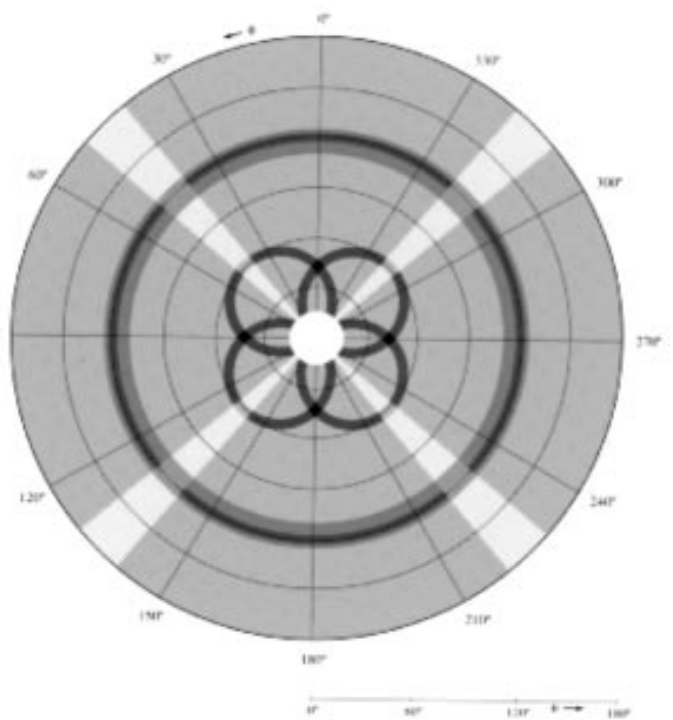


Fig. 7. FSL model of the antenna pattern ($16^\circ \leq \theta \leq 180^\circ$) for the Dwingeloo telescope, corresponding to the situation during the survey. The model was derived from the geometry of the telescope. The antenna pattern published by HBDG (see Figs. 5 and 6) was used to determine the global characteristics of the main features: the spillover ring, the four stray cones, and the shadowing of the support legs

was generally comparable to, or less than the rms baseline uncertainties (~ 0.05 K).

Lockman et al. (1986, hereafter LJM) effectively demonstrated the need for stray-radiation corrections to HI spectra observed with a low-noise receiver, especially in directions of low total HI column densities. They developed a method of correcting the stray-radiation contamination in spectra observed with the NRAO 140-ft telescope. High-angular-resolution (HPBW = $21'$) HI maps were smoothed with the beam pattern of the Bell Labs telescope, and compared with the data from the Bell Labs survey. Differences between the two maps were interpreted as due to stray radiation in the 140-ft telescope data. By applying a bootstrapping method, the stray-radiation contamination in the original spectra was reduced by an order of magnitude. The LJM technique has been used satisfactorily on the 140-ft telescope, with a variety of different receivers (see also Murphy 1993).

The main practical limitation to the bootstrapping method may reside in the 2.5 effective spatial resolution of the Bell Labs data, as well as in its rather coarse effective velocity resolution of $\Delta v = 10.0$ km s $^{-1}$. Benefits and

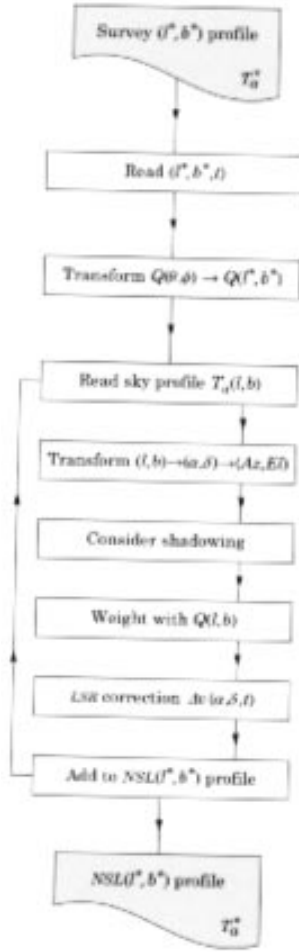


Fig. 8. Schematic diagram of the NSL correction algorithm. The NSL contribution for a survey spectrum at (l^*, b^*) is computed as the convolution of the input sky with the kernel function Q represented in Fig. 4. The notation (l^*, b^*) distinguishes the specific direction undergoing correction from the general directions in the input sky given by (l, b)

limitations of this algorithm are discussed further in Sect. 2.2.

2. Correction algorithm

We report here our modification of the KSCA which was originally developed for the Effelsberg 100-m telescope (Kalberla 1978; Kalberla et al. 1980, hereafter KMR). The modified algorithm was used to correct the spectra in the Leiden/Dwingeloo survey. The KSCA is reviewed in Sect. 2.1; for more details see Kalberla (1978). In Sect. 2.2, a comparison is made with other methods of remedying stray-radiation contamination.

This section describes the method in general. The practical implementation, the modeling of the Dwingeloo telescope characteristics, and the application to the Leiden/Dwingeloo observations are discussed in Sect. 3.

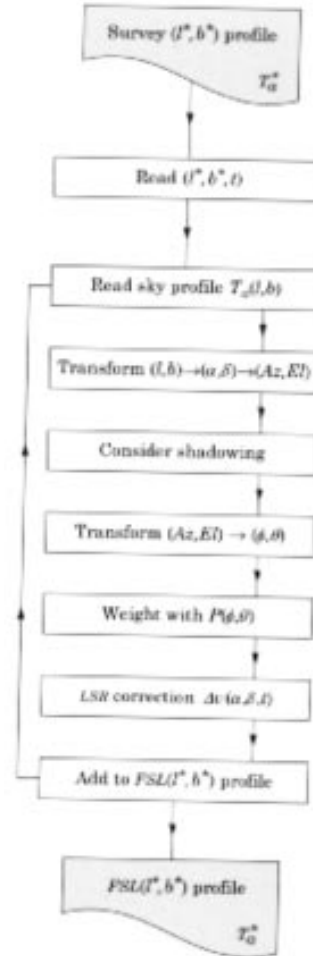


Fig. 9. Schematic diagram of the FSL correction algorithm. The FSL stray-radiation contribution for a survey spectrum at (l^*, b^*) is computed from the convolution of all sky cells above the horizon with the individual (and possibly coincident) features in the FSL antenna-pattern model (indicated by P) shown in Fig. 7

2.1. Description of the method

Observations made with a radio telescope yield sky brightness measurements that incorporate the complete instrumental response. The observed antenna temperature T_a is the convolution of the antenna pattern P with the true brightness distribution on the sky, T . Although the convolution must be applied in *spherical* coordinates we will outline the method using Cartesian coordinates, (x, y) . The integral form of the convolution in these coordinates was given by Bracewell (1956) as

$$T_a(x, y) = \int P(x - x', y - y') T(x', y') dx' dy', \quad (7)$$

where the antenna pattern, $P(x, y)$, is normalized to unity so that

$$P(x, y) dx dy = 1. \quad (8)$$

If the antenna pattern is separated into the main beam (MB) component and the stray pattern (SP) component, then Eq. (7) can be written as $T_a(x, y) = T_{\text{MB}}(x, y) + T_{\text{SP}}(x, y)$, or

$$T_a(x, y) = \int_{\text{MB}} P(x - x', y - y') T(x', y') dx' dy' + \int_{\text{SP}} P(x - x', y - y') T(x', y') dx' dy'. \quad (9)$$

Because we do not want to restore any variations of T inside the main beam, we introduce the main beam efficiency

$$\eta_{\text{MB}} = \int_{\text{MB}} P(x, y) dx dy. \quad (10)$$

The object of the correction algorithm is to obtain the brightness temperature, T_b , which we approximate by

$$T_b = \frac{T_a}{\eta_{\text{MB}}}. \quad (11)$$

Using Eqs. (9) and (10), T_b expands to

$$T_b(x, y) = \frac{1}{\eta_{\text{MB}}} T_a(x, y) - \frac{1}{\eta_{\text{MB}}} \int_{\text{SP}} P(x - x', y - y') T_b(x', y') dx' dy'. \quad (12)$$

To solve this equation, we need the (unknown) sky distribution of T_b . It is possible to use an iterative approximation by replacing $T_b(x', y')$ on the right hand side of Eq. (12) by $\frac{T_a(x', y')}{\eta_{\text{MB}}}$, according to Eq. (11), and then substituting the result in the next iteration.

Such an effort is, however, unnecessary. Equation (12) represents a Fredholm integral of the second kind, which can be solved for $\eta_{\text{MB}} > 0.5$. The solution can be obtained in a single step, using a modification of the antenna pattern $P(x, y)$; details on the derivation of this result may be found in Kalberla (1978). The solution is given by

$$T_b(x, y) = \frac{1}{\eta_{\text{MB}}} T_a(x, y) - \frac{1}{\eta_{\text{MB}}} \int_{\text{SP}} Q(x - x', y - y') T_a(x', y') dx' dy'. \quad (13)$$

Here Q is the so-called resolving kernel function,

$$Q(x, y) = \sum_{i=0}^N (-1)^i K_i(x, y), \quad (14)$$

and K is defined as

$$K(x, y) = \begin{cases} 0 & \text{inside the main beam;} \\ \frac{1}{\eta_{\text{MB}}} P(x, y) & \text{outside the main beam.} \end{cases}$$

Using recursion, we obtain

$$\begin{aligned} K_0(x, y) &= K(x, y) \\ K_{i+1}(x, y) &= \int K_i(x', y') K(x - x', y - y') dx' dy'. \end{aligned} \quad (15)$$

Numerical calculations for $\eta_{\text{MB}} = 0.7$ show that convergence is generally achieved for $N \geq 20$.

2.2. Comparison with other methods

A direct estimate of the incident stray radiation can be obtained by blocking the main beam of the telescope. This can be achieved by pointing the telescope at the Moon. The ubiquity of galactic HI implies that there is a lunar occultation at all times. Depending on the extent of the main beam, the Moon may cover also the nearest diffraction sidelobes, as is the case for the 100-m Effelsberg telescope. Comparing calculated stray profiles with lunar occultation observations, KMR found discrepancies that could be explained by the reflection of the HI sky off the lunar surface. The residuals were consistent with a lunar albedo of 0.07 and a HPBW of about 60° (considering the Moon as a transmitting antenna). Direct evidence for lunar 21-cm reflections had been mentioned by Giovanelli & Haynes (see KMR), who used the Arecibo telescope to observe the Moon at 21-cm. They reported the presence of an emission component that was not observed when the Moon was absent. The velocity of the component was found to correspond to the relative LSR velocity shift between opposite pointing directions of the telescope. Therefore, it seemed plausible that HI emission was being observed at $v_{\text{LSR}} = 0$ km s $^{-1}$ from the direction opposite the telescope main-beam pointing, reflected off the Moon.

Unfortunately, the method of lunar occultation cannot be used for the determination of the stray-radiation contributions at high galactic latitudes. There, lunar reflections add about 50% to the total intensity observed with the Moon absent. Uncertainties in the ‘‘lunar antenna pattern’’, namely the direction and the reflectivity for incident 21-cm radiation, make it impossible to distinguish reliably between lunar reflections and stray-radiation residuals.

An estimate of the mean stray radiation can be obtained from the comparison with observations from telescopes with low side-lobe levels, such as the Bell Labs telescope. The Bell Labs HI survey has been utilized for this purpose by LJM, as discussed in Sect. 1.3.

The main advantage of the LJM correction procedure is that no knowledge is required about the antenna pattern of the telescope for which the profiles are corrected.

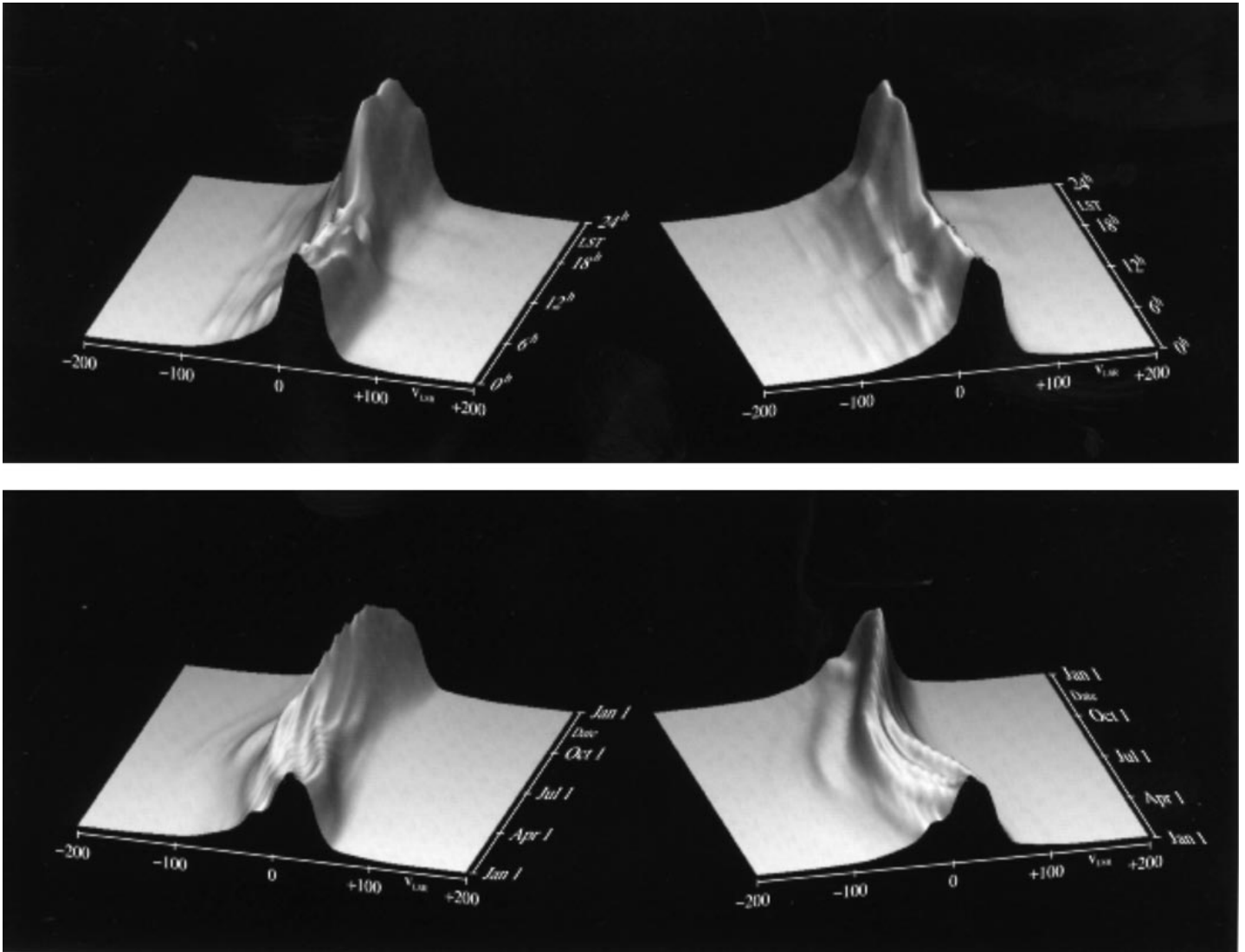


Fig. 10. (upper): Diurnal variations in the FSL stray-radiation contamination expected at $(l, b) = (160^\circ, +50^\circ)$ over a 24-hour (sidereal time) period. FSL profiles were calculated for 1 January, 1994, in steps of one hour in LST. The spectra are displayed as surface plots, viewed from two different angles. The peak temperature in the FSL spectra ranges from 0.41 K (LST= 13^h) to 0.78 K (LST= 17^h). (lower): Seasonal variations in the FSL stray-radiation contamination expected at $(l, b) = (160^\circ, +50^\circ)$ over a year. The FSL profiles were calculated at LST= 6^h04^m (culmination) in steps of about 15 days. The spectra are displayed as surface plots, viewed from two different angles. Peak temperatures range from 0.28 K (15 April) to 0.60 K (15 October). Note the curvature in velocity of the peaks over the course of a year; this is due to the changes in the LSR velocity correction because of the Earth's revolution around the Sun

A major disadvantage, however, is that only the mean stray radiation can be determined. Fluctuations due to changes in the position angle of the telescope are not accounted for. This largely restricts the application of the algorithm to equatorially mounted telescopes, for which the antenna pattern has a fixed orientation with respect to the sky. Furthermore, the correction procedure will only work properly when at least a field of some 2° in extent is observed. The method is unsuited for the determination of the stray radiation in single, pointed observations.

Willacy et al. (1993) used Staveley-Smith's (1985) adaptation of the KSCA to correct observations of the region of low HI intensities discussed by LJM, made with the Mark IA (Lovell) telescope at Jodrell Bank. The Bell Labs survey served as the input sky for the correction procedure. Stray profiles were calculated for $|v_{\text{LSR}}| \leq 100 \text{ km s}^{-1}$ only. Willacy et al. reported that the correction is affected by the presence of saturation effects in the spectra of the Bell Labs survey, for directions in which the peak temperatures exceed 40 K. As a result, they find uncertainties in the stray profiles of $\Delta T \sim 0.4 \text{ K}$, or

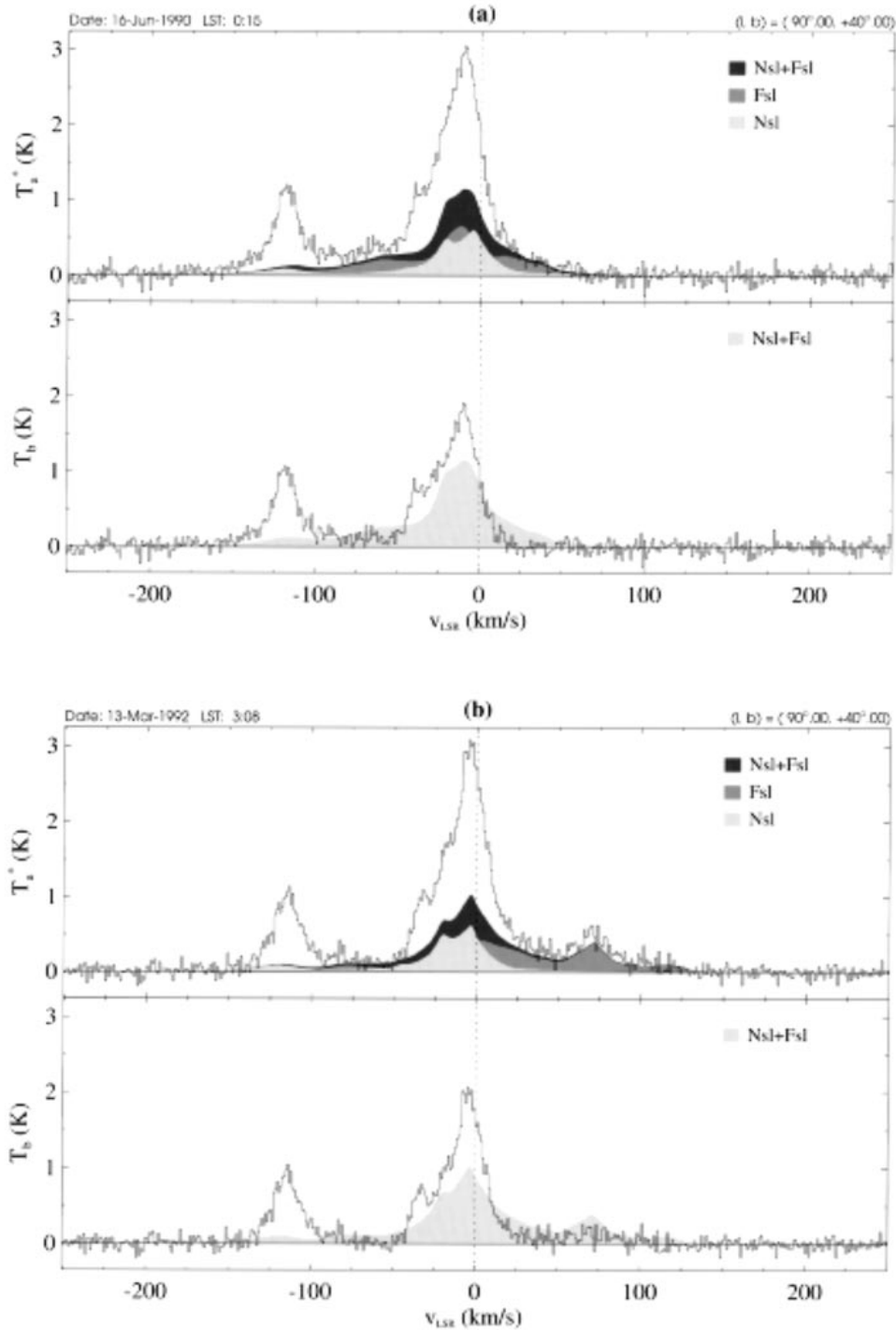


Fig. 11. Stray radiation in two spectra observed towards the direction $(l, b) = (90^\circ, 40^\circ)$. **a)** Spectrum observed in June, 1990. The uncorrected spectrum and the stray profiles are shown in the upper panel. The NSL contribution contains a component that is caused by the HVC near $v_{\text{LSR}} = -115 \text{ km s}^{-1}$. After correction (lower panel) there is hardly any emission left between the HVC and the low-velocity gas. The wing near $v_{\text{LSR}} = -60 \text{ km s}^{-1}$ was due to the FSL stray radiation. **b)** Observation made in March, 1992. A prominent feature of 0.5 K peak temperature is seen in the uncorrected spectrum (upper panel) near $v_{\text{LSR}} = +70 \text{ km s}^{-1}$. The calculated FSL profile proves this to be completely attributable to stray radiation. After correction (lower panel) the feature has disappeared. There seems to be no emission between $v_{\text{LSR}} = -50 \text{ km s}^{-1}$ and the HVC near $v_{\text{LSR}} = -115 \text{ km s}^{-1}$. The details of the origin of the FSL stray-radiation contamination can be seen from Fig. 12

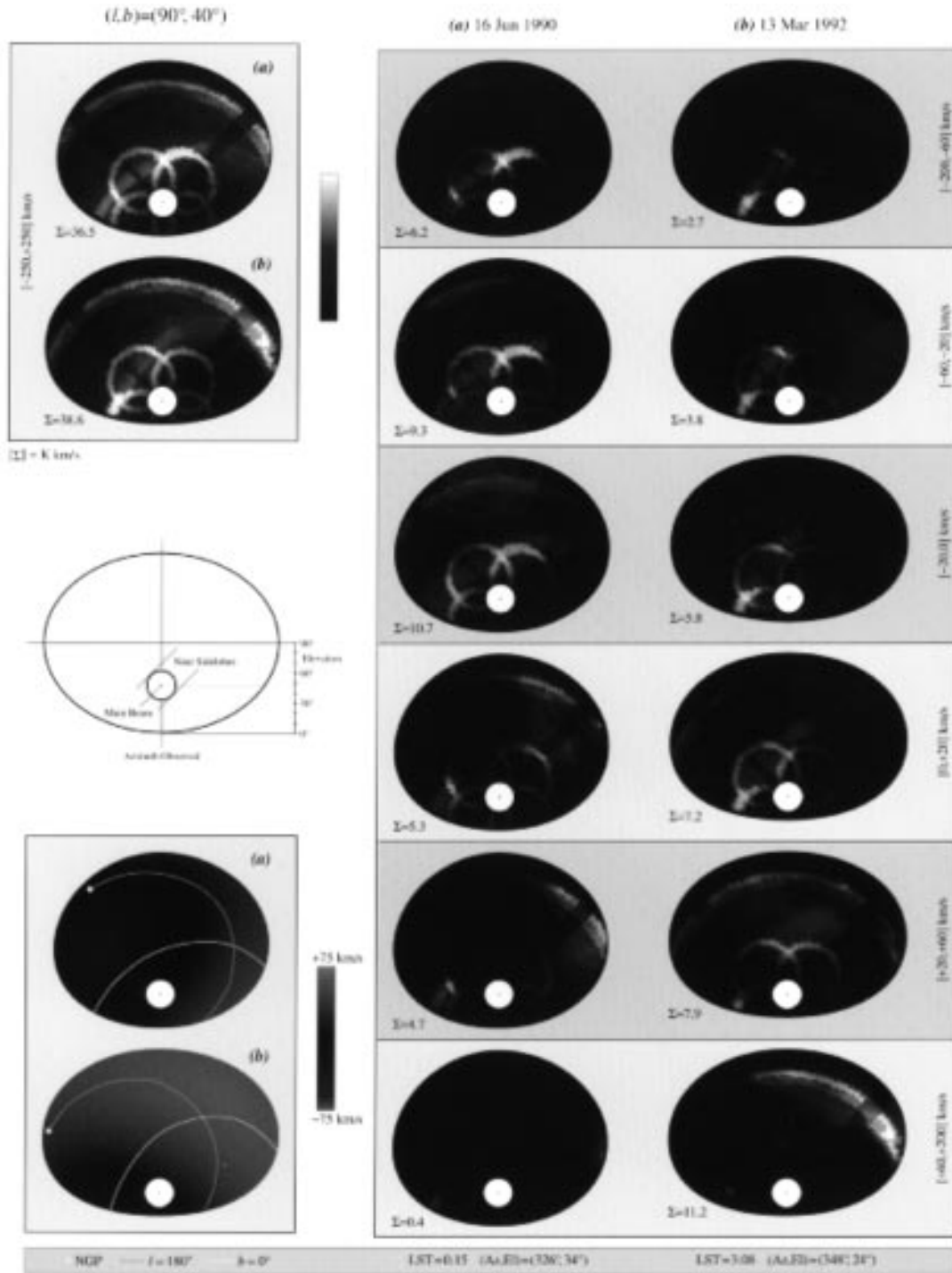


Fig. 12. Stray-radiation spheres for two observations toward $(l, b) = (90^\circ, +40^\circ)$. (upper left) Convolution of the FSL pattern with the HI sky, integrated over the entire velocity range of the correction. (center left) Orientation of the spheres. The center corresponds to the zenith; the circumference represents the horizon. Each sphere displays the full 2π rad² of the visible sky at the time of observing. The position of the main beam (dot) represents the (Az, El) of the observation. (lower left) LSR velocity correction with respect to the direction of the main beam. The galactic plane and north pole are indicated, as is the line $l = 180^\circ$. (right) Six pairs of stray spheres, each for a distinct velocity interval. The scaling is relative to the total FSL stray radiation. The integrated intensities are indicated in units of K km s^{-1} . The sensitive features in the FSL pattern and the bright regions on the sky are clearly visible. Sect. 4.1 explains the interpretation of the stray spheres in relation to the spectra in Fig. 11

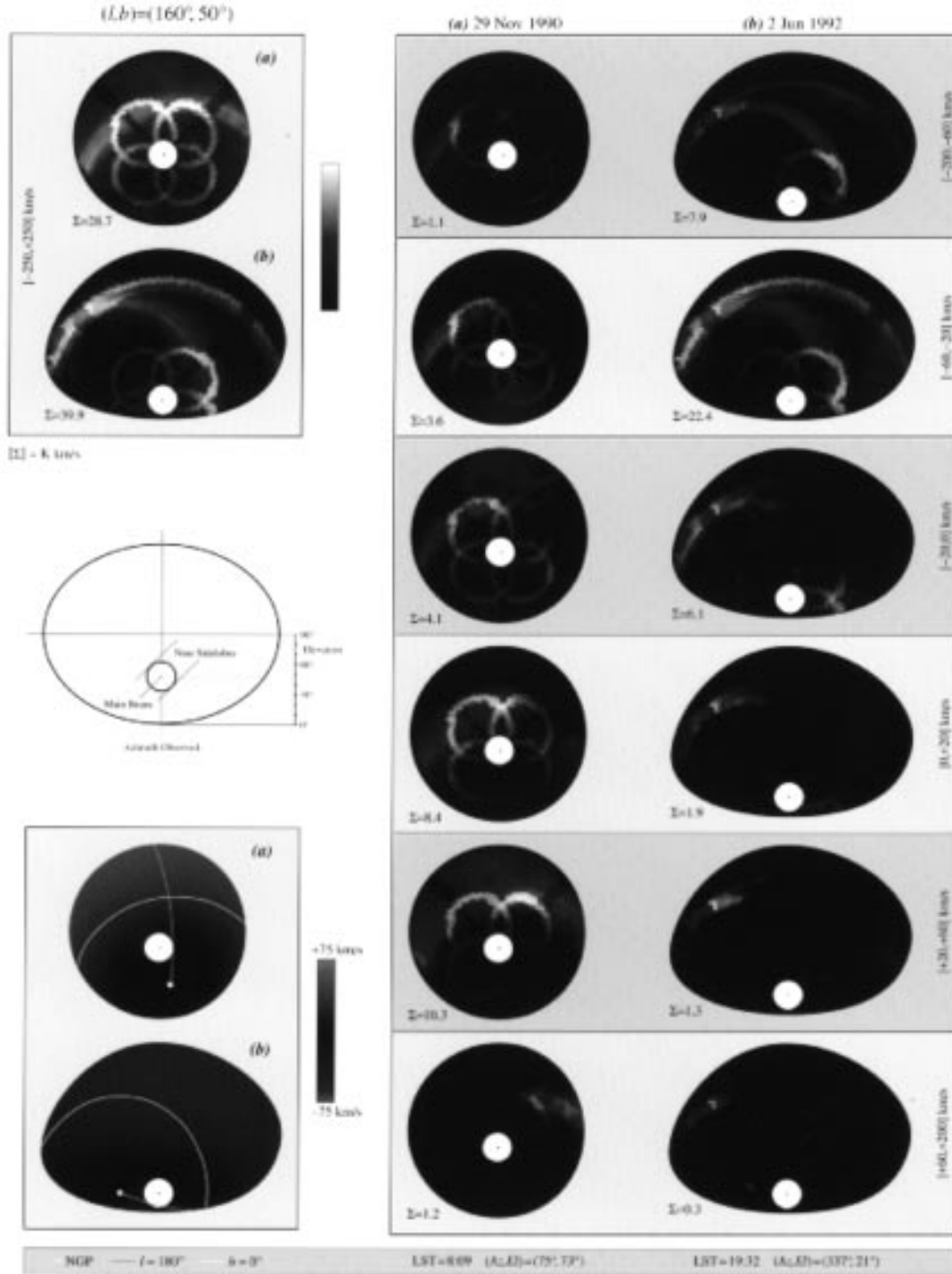


Fig. 13. Stray-radiation spheres for two observations of $(l, b) = (160^\circ, +50^\circ)$. (upper left) Convolution of the FSL pattern with the HI sky, integrated over the entire velocity range of the correction. (center left) Orientation of the spheres. The center corresponds to the zenith; the circumference represents the horizon. Each sphere displays the full 2π rad² of the visible sky at the time of observing. The position of the main beam (dot) represents the (Az, El) of the observation. (lower left) LSR velocity correction with respect to the direction of the main beam. The galactic plane and north pole are indicated, as is the line $l = 180^\circ$. (right) Six pairs of stray spheres, each for a distinct velocity interval. The scaling is relative to the total FSL stray radiation. The integrated intensities are indicated in units of K km s^{-1} . The sensitive features in the FSL pattern and the bright regions on the sky are clearly visible. We explain in Sect. 4 the interpretation of the stray spheres in relation to the spectra shown in Fig. 14

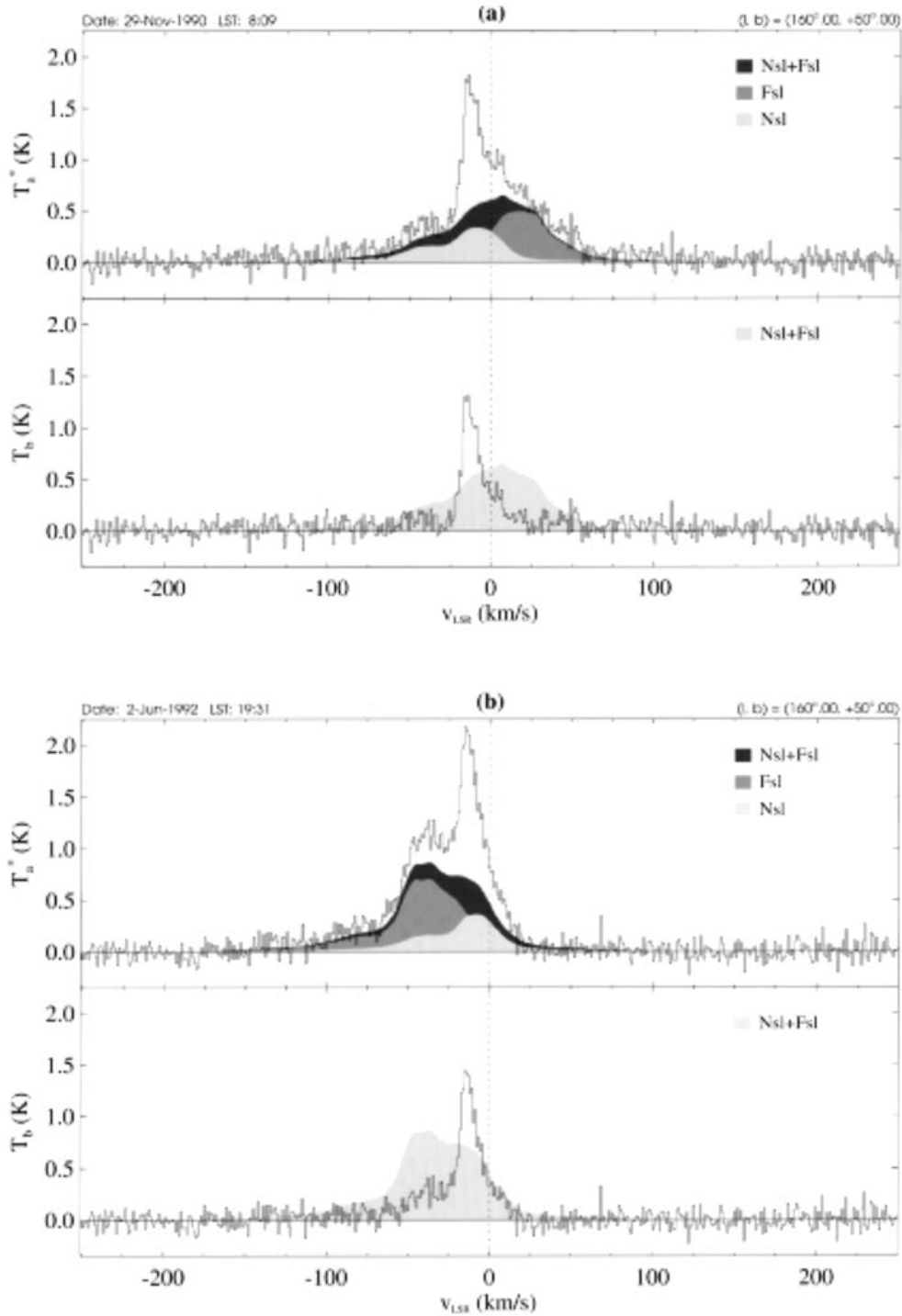


Fig. 14. Two dissimilar spectra resulting from separate observations towards $(l, b) = (160^\circ, +50^\circ)$. The FSL profile dominates the stray radiation at high $|b|$. The stray radiation can exceed 50% of the total emission in directions of low column density. This is seen in the lower panel in each pair, where the stray profiles (shaded) contain more emission than the main beam; the far sidelobes dominate the shape and intensity of the uncorrected profile. **a)** Observation made in November, 1990, at high elevation (73°). The FSL profile is less prominent than in **b)**, because the spillover ring is on the ground rather than towards the sky. FSL emission with a peak temperature of 0.5 K is found near $+115$ km s $^{-1}$. **b)** Spectrum observed in June, 1992, at an elevation of 21° . Here the spillover ring is directed towards the sky. A negative-velocity shoulder is present in the uncorrected spectrum, with a peak temperature of about 0.7 K near $v_{\text{LSR}} = -40$ km s $^{-1}$ and extending to $v_{\text{LSR}} = -150$ km s $^{-1}$. Figure 13 clarifies the difference in FSL contamination between the two spectra

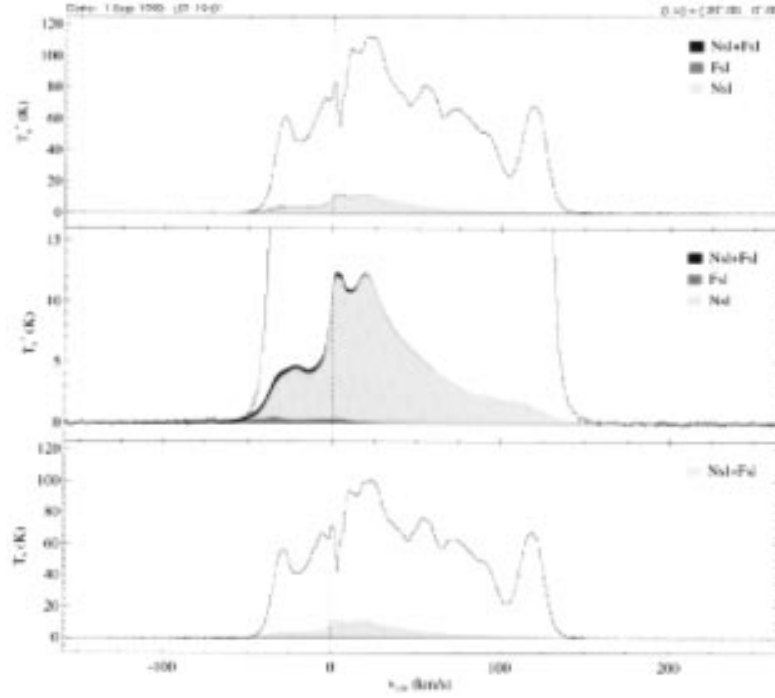


Fig. 15. Demonstration that stray radiation near the galactic plane is dominated by the NSL contribution. For the uncorrected profile (upper panel), the NSL profile contains about 15% of the total emission. When the scaling is enlarged (center), the FSL contribution is clearly seen to be relatively insignificant in regions of high intensity

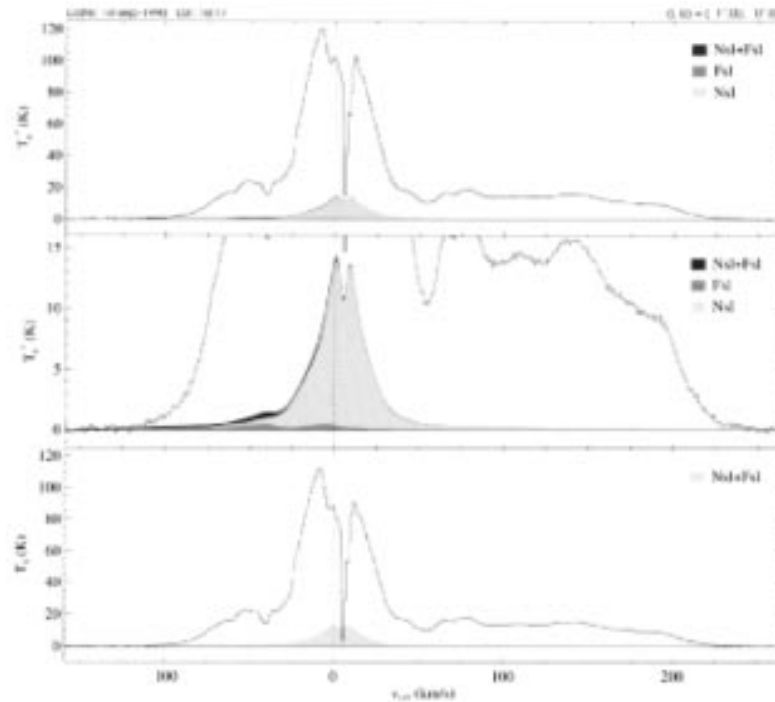


Fig. 16. Demonstration that the NSL's near the galactic center contain an absorption signature that is present in the spectrum at $v_{\text{LSR}} = 6 \text{ km s}^{-1}$. After correction (lower panel), the absorption in the spectrum is more prominent. Correction for stray radiation generally sharpens all spectral features, whether due to emission or to absorption

$\Delta N_{\text{HI}} \sim 10^{19} \text{ cm}^{-2}$. Comparing their spectra to those toward two positions measured by LJM and by Jahoda et al. (1990), they estimated that these uncertainties had propagated as systematic offsets of $\sim 15\%$ in the calculated total column densities. The saturation effects in the Bell Labs data were analyzed by Kuntz & Danly (1992), who compared the spectra of four IAU standard sources with the calibration measurements of Williams (1973). They found that “... peak brightness temperatures ... must be increased by only [*sic*] a factor of 1.1 to 1.6 to match the true brightness temperatures”.

It will perhaps clarify matters if we note that the stray-radiation correction applied here differs in principle from the CLEAN algorithm commonly applied to measurements made using an interferometer. The contrast from point to point in the HI sky is very much lower than the contrast in the continuum sky at decimetric wavelengths; furthermore, HI is everywhere, not confined to point sources. Thus the general structure of the antenna pattern is important, not only the individual side lobes.

3. Correcting the Leiden/Dwingeloo survey for stray radiation

The Dwingeloo telescope has an elevation–azimuth mounting, and therefore the stray radiation in the survey spectra cannot be removed using the LJM algorithm, for which an equatorial mounting is a necessary requirement. We demonstrate in this article the effectiveness of convolving the antenna pattern with an input HI sky, following the KSCA.

As Van Woerden had shown in the early years of the Dwingeloo telescope, stray radiation effects could be estimated from consideration of the sensitive features in the antenna pattern and the sky brightness distribution (see Sect. 1.2). Kalberla had used the Dwingeloo antenna pattern measured by HBDG to determine the properties of stray cones and spillover regions, and subsequently to model the antenna pattern of the Effelsberg 100–m telescope accordingly.

The two necessary requirements for the application of the KSCA are the total visible HI sky brightness distribution, and the detailed antenna pattern of the Dwingeloo telescope. Section 3.1 describes the creation of an input sky from the uncorrected survey data, and Sect. 3.2 discusses determination of the antenna pattern parameters. The antenna pattern is divided into three parts: main beam (MB), near sidelobes (NSL), and far sidelobes (FSL). The NSL and FSL regions together make up the stray pattern, namely $\text{SP} = \text{NSL} + \text{FSL}$. Section 3.3 presents the model for the NSL area that was created from holographic measurements of the WSRT telescopes. The model for the FSL pattern is described in Sect. 3.4. The computer implementation of the KSCA is discussed in Sect. 3.5.

3.1. Input sky model

The input HI sky used to correct Effelsberg 100–m telescope spectra in the original application of the KSCA was the combined Berkeley survey (Weaver & Williams 1973; Heiles & Habing 1974). The velocity coverage of this material is limited (250 km s^{-1} for $|b| \leq 10^\circ$ and effectively less than 100 km s^{-1} for $|b| \geq 10^\circ$), and the rms sensitivity is only about 0.5 K. The KSCA adapted at Jodrell Bank used as input sky the Bell Labs survey, which has excellent sensitivity rms $\sim 0.05 \text{ K}$, good velocity coverage (654 km s^{-1}), but poor velocity resolution ($\Delta v = 10.0 \text{ km s}^{-1}$), and coarse effective angular resolution ($2''.5$). Moreover, as already mentioned, the Bell Labs survey suffers from some saturation effects at $T_a > 40 \text{ K}$.

The most robust stray–radiation correction required using the HI input sky from the (uncorrected) Leiden/Dwingeloo survey. The correction could therefore only be applied after the entire accessible sky had been observed. The Leiden/Dwingeloo survey improves upon the Berkeley surveys in all relevant parameters except positional resolution. The advantages over the Bell Labs survey lie in the higher velocity resolution and greater dynamic range; the better spatial resolution of the Hartmann & Burton survey is irrelevant in this context, because the input sky was created as $2^\circ \times 2^\circ$ cells. Re–binning the Dwingeloo data to the same resolution improves its sensitivity beyond that of the Bell Labs survey. The Bell Labs data are, of course, *initially* a better estimate of the true sky brightness (for $T \leq 40 \text{ K}$, in any case) due to the lack of stray radiation received by the horn reflector. However, it was assumed that the spectral details of the stray radiation would disappear when the individual contributions of all spectra in the stray–pattern solid angle Ω_{SP} were convolved with the antenna pattern. Therefore the influence of the stray radiation present in the input sky may be approximated by η_{SP} .

The initial reduction of the Dwingeloo spectra which were used to create the input sky has been described by Hartmann (1994) and by Hartmann & Burton (1996). Further preparation for the stray–radiation correction proceeded as follows. The homogeneous all–sky data cube that was created from the reduced spectra (see Sect. 3.3), was binned into cells of three different sizes. The size of the cells was principally determined by the computer implementation of the algorithm. Near the galactic plane ($|b| \leq 1^\circ$), the data were binned into cells of size $\Delta l \times \Delta b = 2^\circ 0' \times 1^\circ 5'$, centered on $(l, b) = (0^\circ 25' + N \times 2^\circ, 0^\circ 0')$ [$N = 0, \dots, 179$], and each filling solid angles $\Omega = 9.14 \cdot 10^{-4} \text{ rad}^2$. In the galactic polar caps ($|b| \geq 88^\circ 75'$), the sky cells measured $2^\circ 0' \times 1^\circ 25'$, were centered on $(l, b) = (1^\circ 25' + N \times 2^\circ, \text{sgn}(b) \times 89^\circ 375')$ [$N = 0, \dots, 179$], and had $\Omega = 3.74 \cdot 10^{-4} \text{ rad}^2$. For the latitude range $1^\circ 0' \leq |b| \leq 88^\circ 75'$, the sky cells measured $2^\circ 0' \times 2^\circ 0'$, and were centered on $(l, b) = (1^\circ 25' + N \times 2^\circ, \text{sgn}(b) \times (1^\circ 75' + M \times 2^\circ))$, [$N = 0, \dots, 179; M = 0, \dots, 43$]. The solid angles filled by

these cells range from $\Omega = 8.61 \cdot 10^{-4} \text{ rad}^2$ (at $|b| = 87^\circ 75'$) to $\Omega = 1.22 \cdot 10^{-3} \text{ rad}^2$ (at $|b| = 1^\circ 75'$).

The spectra binned into these cells were averaged with unit weights and clipped to 512 channels covering a velocity range of $|v_{\text{LSR}}| \leq 264 \text{ km s}^{-1}$. The input sky consisted of 8071 profiles, each representing a cell of specified position and solid angle, and occupied 16 Mbytes of memory or disk space.

3.2. Antenna pattern of the Dwingeloo 25-m telescope

Accurate empirical determination of an antenna pattern is difficult, due to large uncertainties in the measurement of the appropriate parameters (see Baars 1973). We used all available data on the calibration of the Dwingeloo receiver and feed. These data included hot/cold calibrations at 1611 MHz, using a scaled feed. In addition, we measured the total-power response of strong continuum sources (Cas A, Cyg A, Vir A, Tau A, and the Sun) away from the main beam, to determine some crude characteristics of the antenna pattern.

A nearly complete map of the Dwingeloo antenna pattern was published by HBDG. By joining the 25-m paraboloid with a nearby 7.5-m Würzburg antenna, they created an interferometer to measure the antenna response at 1415 MHz. For some 19 000 points in the pattern, representing about 60% of a complete sphere, the response to strong radio sources was measured. (Mapping the antenna pattern to the completeness that HBDG attained was a major effort, requiring some 1500 hours of observing time.) The results were presented in the form of contour maps of attenuation levels (in 2.5 dB increments) relative to the power received in the main beam. The shape of the main beam was determined separately, to a level of -20 dB .

Although the feed-support structure of the telescope was changed from three to four legs shortly after the experiment, the HBDG maps (shown in Figs. 2, 5, and 6) were still of great value for the determination of the current antenna pattern characteristics.

3.3. Modelling the near sidelobes

The antenna pattern of the Dwingeloo telescope within a radius of 6° from the beam axis ($\theta = 0^\circ$) is shown in Fig. 2. When measured by HBDG, the main beam was found to be slightly elliptical, with HPBWs of $0^\circ 57' \times 0^\circ 62'$. No sharp “null” separated the main beam from the first diffraction sidelobe.

To determine the current total NSL response (defined to extend to $\theta = 16^\circ$) of the Dwingeloo telescope, we used holographic beam measurements from the WSRT of 3C84 at 6-cm wavelength, which were kindly provided by Van Someren Greve (1991). The amplitudes of the measurements for 12 telescopes were averaged, auto-correlated, and Fourier transformed. After scaling with respect to the wavelength, these data were used as the basis for a model

of the NSL pattern. Figure 3 shows a gray-scale image of the mean WSRT pattern, logarithmically scaled between 70 dB and 20 dB below the main beam sensitivity. There are two principal justifications for the generalization of the mean WSRT pattern to that of the Dwingeloo telescope. First, the geometry of the antenna in Dwingeloo is quite similar to that of the antennas in Westerbork. (It is not relevant in this regard that the Dwingeloo mounting is an elevation-azimuth one, while the WSRT mountings are equatorial.) Second, as mentioned above, the feed-support structure of the Dwingeloo telescope was modified to accommodate a new generation of front-ends built for the WSRT. This changed the aperture efficiency and the main beam efficiency from the values determined by HBDG. The Dwingeloo feed is currently of similar design to that of the WSRT feeds.

The solid angle of the main beam, defined as the beam width between first nulls (see Sect. 1.1), was determined as $\text{BWFN} = 0^\circ 9'$. The outer limit of the NSL region was mainly determined by the computer implementation of the algorithm (see Sect. 3.5). Accordingly, we chose the NSL pattern as the region bounded by $0^\circ 9' \leq \theta \leq 16^\circ$, which incidentally appropriately determines $\eta_{\text{NSL}} \sim 0.5\eta_{\text{SP}}$. The WSRT pattern was converted to the kernel function of Eq. (14), and divided into 468 cells (see Fig. 4). Each cell is described by its extent (in polar coordinates), solid angle, and sensitivity. We calibrated the sensitivity scale of the model by observing the total-power response of Cas A in the NSL pattern of the Dwingeloo telescope.

3.4. Modelling the far sidelobes

The antenna pattern beyond $\theta = 16^\circ$ was not determined by direct observations. The option to connect the 25-m telescope to a reference antenna, creating a two-element interferometer (as HBDG had done) no longer existed. (The Würzburg antenna in Dwingeloo was dismantled during the course of the survey observations work, and donated by the NFRA to the Deutsches Museum in Munich). Without interferometry, the antenna pattern could not be determined below a level of about -30 dB , whereas sensitivity to -60 dB is needed for an accurate stray-radiation determination. This can be argued as follows. Assume a homogenous HI sky distribution, and a homogeneous FSL pattern, which has a constant sensitivity of -60 dB compared to the main beam. At any given moment, half of the FSL pattern is directed towards the sky, and therefore $\Omega_{\text{sky}} = 2\pi \text{ rad}^2$ at -60 dB will receive radiation. This integrates to $\sim 3\%$ of the power received in the main beam.

We derived a model of the FSL pattern from the geometry of the Dwingeloo telescope. Considering the geometry of the Effelsberg telescope, Kalberla (1978) had found three major features that contributed to the FSL antenna pattern of the 100-m, namely a spillover ring, four stray cones, and the apex cabin. It was expected that the spillover ring and the stray cones (radiation scattered off

the feed–support legs) would be present in the Dwingeloo pattern as well; the 25–m telescope has no apex cabin. Such components had indeed been seen by HBDG. Figures 5 and 6 represent the FSL patterns determined by HBDG.

Figure 6 shows the rear half of the antenna pattern. Only the same ϕ –range as in the outer parts of the Fig. 5 was mapped. The spillover ring is dominant. It is centered around $\theta = 120^\circ$, and has a mean sensitivity that lies about 5 dB above the surrounding regions. The edge of the reflector was at $\theta = 125^\circ$.

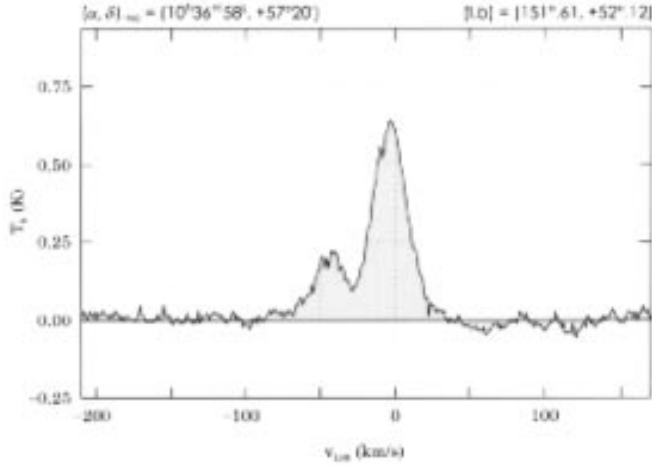


Fig. 17. Spectrum in the direction of the lowest known HI column density on the sky (the LJM Hole: $N_{\text{HI}} = 4.4 \cdot 10^{19} \text{ cm}^{-2}$), observed with the NRAO 140–ft telescope (beam= $21'$) (Jahoda et al. 1990). The artifacts that are present in the baseline regions are the result of the stray–radiation correction (described by LJM) applied

The forward half ($\theta \leq 90^\circ$) of the Dwingeloo antenna pattern shown in Fig. 5 was completely mapped for $\theta \leq 70^\circ$ and over 40% of the range of ϕ , out to $\theta = 90^\circ$. The stray cones are prominent, and clearly indicate the three–legged feed support structure for the situation in 1968. The centers of the cones are at $\theta = 30^\circ$, for $\phi = 60^\circ$, 180° , and 300° , and their sensitivity is about 6 dB higher than the surrounding average. The three support legs (each about one wavelength in diameter) made an angle of 30° with the reflector axis, and were directed towards $\theta = 150^\circ$ at $\phi = 0^\circ$, 120° , and 240° . For $50^\circ \leq \theta \leq 90^\circ$ in these directions of ϕ , the pattern shows regions of low sensitivity, caused by shadowing of the feed by the support legs. The difference from the average sensitivity of the areas in–between the leg shadows is about 4 dB.

The presence of a spillover ring in the Dwingeloo antenna pattern had been suspected by Van Woerden (1962); this suspicion was later confirmed by direct measurements (see Sects. 1.2 and 1.3). The observed stray cones are in good agreement with theoretical predictions (see Mentzer 1955) on the basis of the supplied geometrical data.

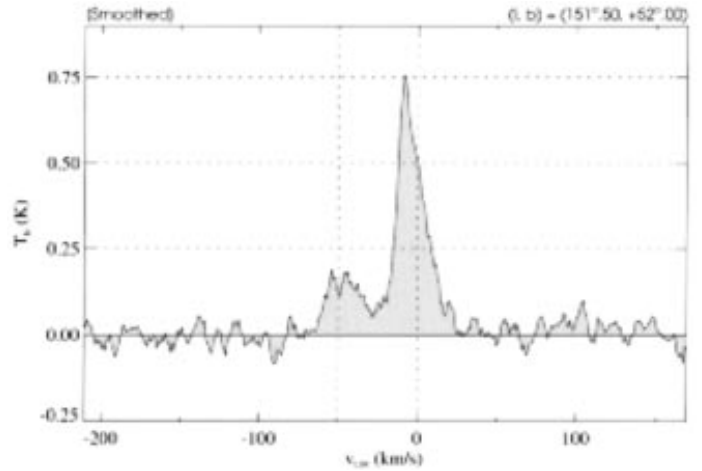


Fig. 18. Spectrum from the Leiden/Dwingeloo survey observed nearest to the position shown in Fig. 17. Although the telescopes, their beam sizes, the receivers, the exact pointing directions, and the methods of stray–radiation correction are different, the spectra agree well. The total column density in this spectrum is $N_{\text{HI}} = 3.7 \cdot 10^{19} \text{ cm}^{-2}$

Unfortunately, the HBDG data could not be used directly as a FSL model, because the telescope dish had been re–surfaced in 1969, and the feed–support structure changed from three to four legs in 1974 (see Sect. 1.3). The re–surfacing of the dish was not expected to cause significant changes in the FSL pattern. Maybe the old mesh ($15 \times 15 \text{ mm}$) was a little more susceptible to penetration of 21–cm radiation than the new, finer mesh ($7.7 \times 7.7 \text{ mm}$). The relevant characteristics, however, are determined by the feed support structure (stray cones), and the position of the rim (spillover). We derived a model of the stray cones and the spillover ring from the present telescope geometry, and used the quantitative data of HBDG as a guideline for the extent and sensitivity of these features. The model was refined by including the shadowing from the support legs. In its final form, the model consists of 23 elements, each described by its extent (in antenna coordinates), and sensitivity. The stray cones were accounted for separately, and added to the total FSL contribution.

Figure 7 shows the FSL model over the entire range $16^\circ \leq \theta \leq 180^\circ$. A general background level is shadowed by the four feed–support legs. The sensitive areas are the spillover ring and the stray cones. In regions where the stray cones overlap, their contributions are added. The smooth appearance of the model is due to the computer implementation.

The first tuning of this FSL pattern model was done by observing the Sun in the stray cones and the spillover ring. These observations confirmed the location of the various FSL features. Calibration of the sensitivity cannot reliably be done by observations of the Sun; more powerful tools

exist to resolve this problem and are discussed in Sects. 4.1 and 4.3.

The discussion below indicates that an important empirical test of the stray-radiation model is afforded by the large number of repeated observations of individual positions. Indeed, such confirmation provided the principal motivation for observing some 10% of the pointed observations more than once, as well as for the numerous measurements of the IAU standard field S7.

3.5. Computer implementation

For every observation entering the Leiden/Dwingeloo HI survey, the NSL and FSL profiles were calculated separately, using a different approach. Only the galactic coordinates (l^*, b^*) , and the date and time of observing, t , were required; in the following discussion, the notation (l^*, b^*) indicates the coordinates of the direction undergoing the stray-radiation correction, while (l, b) denotes the gamut of directions over the input sky. The stray profiles were stored in the same format, and with the same header information as the survey spectra. The source name was modified to reflect the identity of the correction. The code is written in FORTRAN, and was executed on a 150 MHz Alpha-APX (DecStation 3000/500) with 64 Mbytes RAM. The entire HI sky model could be kept in core memory during execution. The calculation of the two stray-radiation profiles required about 1.1 seconds of CPU time; the correction for all the survey spectra required about a week to compute. This program could in principle be applied to other telescopes.

Calculation of the near-sidelobe contribution. The kernel function Q (see Eq. 14) was determined from the model of the NSL antenna pattern, and represents the core of the NSL correction algorithm. Figure 8 shows the schematic data flow of the procedure. From the header of a survey spectrum, l^* , b^* , and t were extracted. The kernel function was converted from antenna coordinates (ϕ, θ) to galactic coordinates, with the main beam direction ($\theta = 0^\circ$) centered on (l^*, b^*) . The procedural loop carried out the convolution of Ω with the input sky. Every sky profile (l, b) inside the NSL region was weighted by $\Omega(l, b)$ and by the relative solid angles of the two elements. For convenience, we call this weighted convolution of an antenna pattern element with a sky cell, the *cross section*. Next, the position was converted to equatorial coordinates, and the LSR correction Δv at t was calculated. This correction corresponds to the difference in LSR velocity between the direction of the main beam (l^*, b^*) and the direction of the input sky cell (l, b) , at the time of observing. The calculated NSL element was added to the total NSL contribution. The loop was finished after all 8071 sky cells had been correlated with the 468 kernel elements.

Calculation of the far-sidelobe contribution. Because of the large extent of the FSL pattern (covering almost a full 4π rad²), it is computationally impractical to convert it to a kernel function and apply the convolution with the input HI sky, as was done for the NSL correction. Instead, the profiles of the input sky were converted to antenna coordinates, and convolved with the FSL features with which they coincided. The schematic correction algorithm is shown in Fig. 9. The relevant observational parameters (l^*, b^*, t) were read from the survey spectrum, and the FSL contribution was calculated by processing all the profiles from the input sky in a loop that carried out the following operations.

The position of the sky profile at (l, b) was converted to (α, δ) , and then to (Az, El) for the time of observation t . The position was checked for obstruction by the horizon, which (even in the Netherlands) is not necessarily at $El = 0^\circ$. The algorithm contained a model of the horizon, in which obstructions (such as hills, in the case of Effelsberg, or woods, in the case of Dwingeloo) could be accounted for. If the sky cell was “up”, it was converted to antenna coordinates (ϕ, θ) . The list of 23 FSL features was searched for positional coincidence. There was always a contribution from the overall background, but in some cases three features overlap (for example at $(\phi, \theta) = (45^\circ, 60^\circ)$, where the background, a stray cone, and a leg shadow are coincident; see Fig. 7). The contributions of all cross sections (the convolution between sky cells and FSL features, weighted with the FSL pattern power, P , and the solid angles) were added. The result was corrected for the LSR velocity shift, and accumulated in the FSL correction profile.

3.6. Discussion of the telescope parameters

The characteristics of the Dwingeloo telescope with the three-legged feed support and the old antenna surface were extensively measured by HBDG. We derived the current parameters from models of the antenna pattern and from various calibration measurements that were made to determine the correctness of the pattern. The results are summarized in Table 1, together with the data taken from HBDG, and the parameters pertaining in 1978 for the Effelsberg 100-m telescope (Kalberla 1978). Estimates of the uncertainty are also given. Comparing the 1968 data with the present, it is clear that the aperture efficiency is much improved. This improvement is largely due to the broader response of the new (1974) corrugated primary feed, which causes a better illumination of the telescope dish. At the same time, it somewhat increased the HPBW of the main beam. This feed served as the prototype for the feeds developed for the WSRT; as that is a synthesis array, the design was optimized to yield a high aperture efficiency, at the expense of a lower main beam efficiency. Presently, the Dwingeloo telescope’s η_{MB} is about 10% lower than it was in 1968, and about equal to that of the

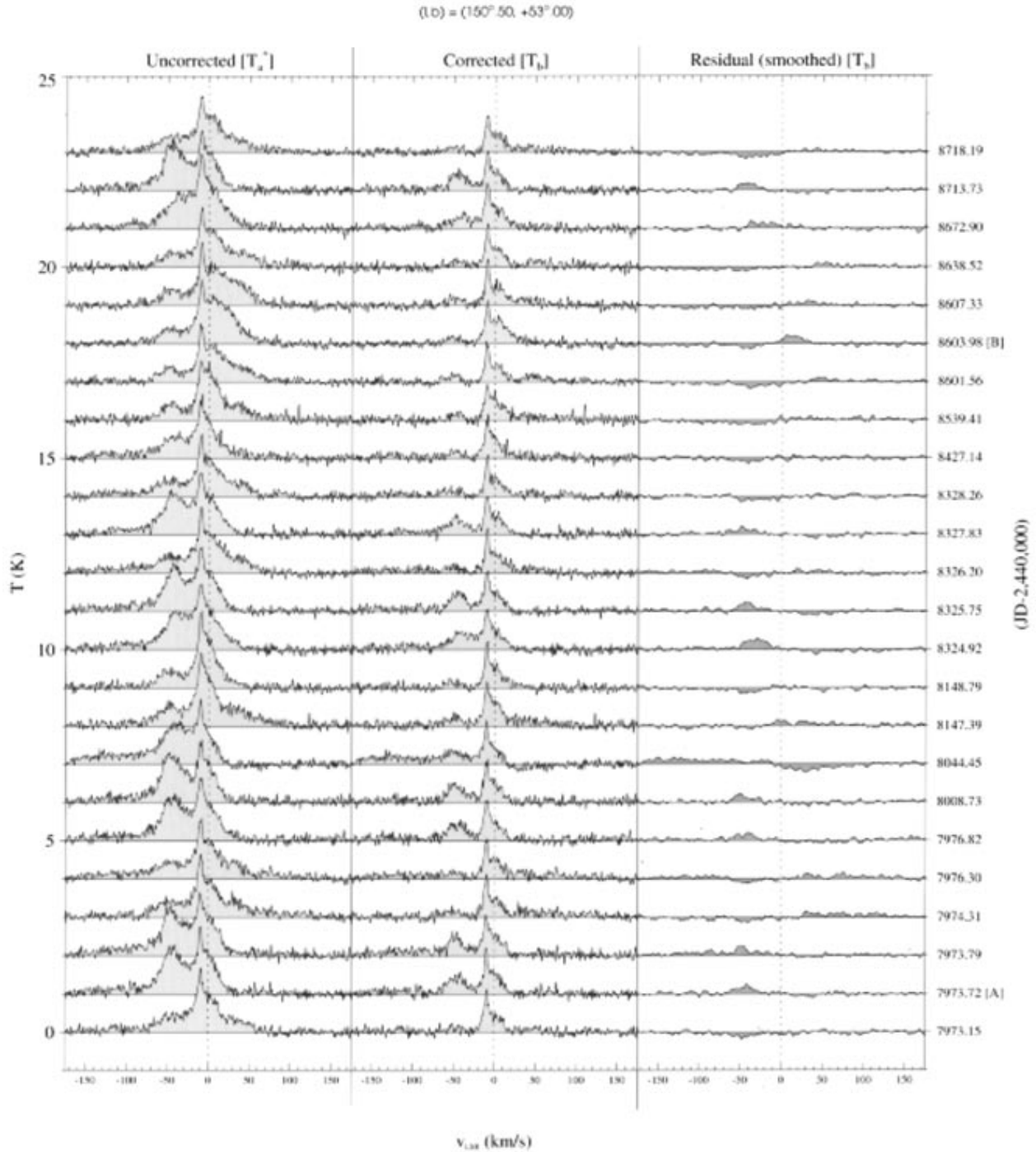


Fig. 19. Spectra from a test suite of 24 observations of a single direction towards the LJM Hole. The Julian Dates indicate the time between observations, ranging from less than a day to about two years. The uncorrected spectra (left) are quite different, due to the variability of the stray-radiation contribution from the far sidelobes. After correction (center) differences are still present. The residuals (right) were obtained by subtracting the mean of the corrected profiles. The spectra labeled [A] and [B] are considered in more detail in Fig. 22 and the accompanying discussion in the text

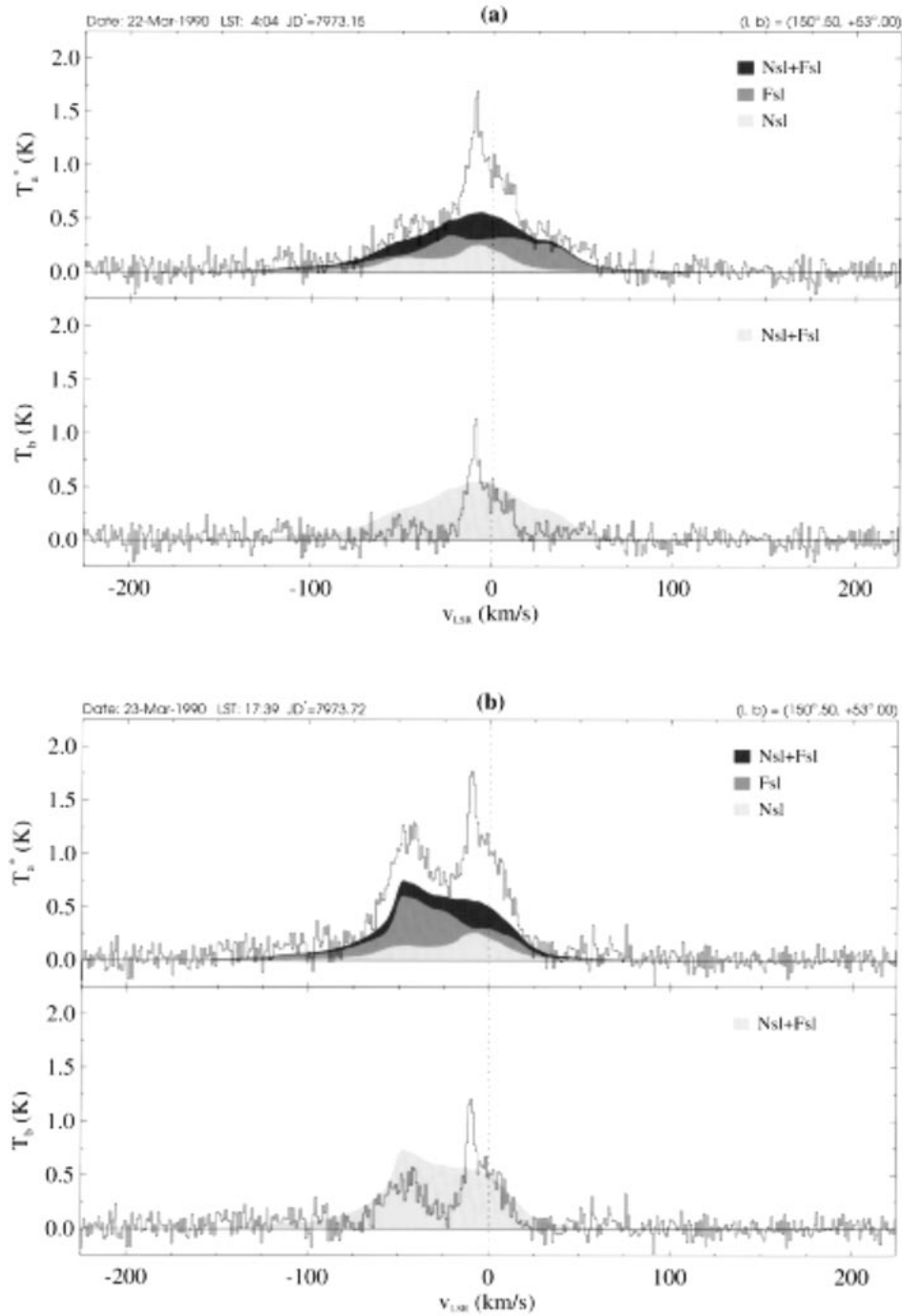


Fig. 20. Stray-radiation contributions for two samples from the test suite of Fig. 19. The time between observation of these spectra was about 13.5 hours. After subtraction of the stray radiation, the profile in **a)** shows no significant emission for $|v_{\text{LSR}}| > 25 \text{ km s}^{-1}$. The corrected profile in **b)**, however, has a prominent feature near $v_{\text{LSR}} = -50 \text{ km s}^{-1}$. Either **a)** was over-corrected, thereby removing a real feature, or **b)** has FSL stray radiation still present. The text addresses both possibilities

Effelsberg telescope. A decrease in η_{MB} implies a higher value of η_{SP} . As can be read from the table, η_{SPILL} has almost doubled, while η_{NSL} has increased by about 30%. The sensitivity of the stray cones remained the same, even though there are now four support legs instead of three.

Table 1. Summary of the main antenna parameters for the Dwingeloo 25-m (both 3 and 4 support legs configurations) and the Effelsberg 100-m telescopes. The data for the three-legged Dwingeloo telescope are taken from HBDG; the Effelsberg parameters, from Kalberla (1978). Values of σ are estimates of the typical uncertainties in the parameters

	Dw(4)	Dw(3)	Effelsberg	σ
epoch	1993	1968	1978	—
feed	4 legs	3 legs	4 legs	—
HPBW	36'4	35'7	9'0	1%
BWFN	54'0	—	11'0	—
NSL radius	16°	—	4°	—
efficiencies:				
aperture	65%	56%	53%	3%
MB	69%	76%	70%	5%
NSL	19%	14%	15%	2%
spillover	4.5%	2.5%	2.5%	0.5%
stray cones	4.0%	4.0%	3.5%	0.5%
apex	—	—	3%	0.5%
background	3.5%	3.5%	6%	0.5%

The parameters describing the Dwingeloo telescope in its current state are consistent with those describing the Effelsberg telescope. Differences reflect differing aspects of the construction of the telescopes. The 100-m has an apex cabin that causes reflections, and therefore distinct features in the FSL pattern. Furthermore, the four feed-support legs contain substructures (such as ladders), which probably cause the higher background level.

The radius that separates the NSL region from the FSL pattern is only 4° for Effelsberg because both the HPBW and the size of the NSL region scale inversely with the telescope diameter (see Baars 1973). The BWFN and the appearance of individual side lobes depend on the details of the antenna design; they were calculated from the Fourier transform of the auto-correlated aperture illumination.

4. Results

In this section, we show examples of the stray-radiation corrections. More attention is given to the FSL profiles than to the NSL ones, because the far-sidelobe situation is more variable with time. Results of repeated observations of the LJM Hole are discussed. Inconsistencies between corrected profiles are analyzed. An additional FSL component is proposed, originating from reflections of the HI sky on the ground. The stray-radiation contributions

for the individual components (expressed in equivalent column densities) are presented at the end of this section.

4.1. Far-sidelobe corrections

The FSL component is the more variable part of the stray-radiation contribution. The cause of time variability of FSL stray radiation depends on the telescope mounting, and is discussed in Sect. 4.1.1. In Sect. 4.1.2 we show simulated FSL profiles illustrating variations with hour angle and season of observing. The method used to tune the far-sidelobe antenna pattern is discussed in Sect. 4.1.3.

4.1.1. Telescope mounting and FSL contamination

As the Dwingeloo telescope has an elevation-azimuth mounting, the orientation of the antenna pattern with respect to the sky is constantly changing. The FSL contribution is mainly determined by the position of the galactic plane (where the HI intensities are everywhere high) with respect to the most sensitive FSL features (the spillover ring and the stray cones). These cross sections determine the total integrated stray intensity received, while the spectral distribution depends on the difference in LSR velocity between the directions of the principal cross sections and the direction of the main beam.

For an equatorially mounted telescope, the FSL time variability depends only on the elevation at the time of observing. The elevation determines if cross sections point to the ground, i.e. whether or not the bright sky cells are below the horizon and thus whether or not the sensitive FSL features (still “pointed” at those sky cells) are projected on the ground. Repeated observations made with identical main-beam pointings, but at various hour angles, will involve the sensitive FSL features in the antenna pattern always pointing in the same direction. Only the position with respect to the horizon determines if the profile will be contaminated by these, otherwise constant, cross sections.

4.1.2. FSL model calculations

The KSCA calculates the stray-radiation contribution on the basis of the models of the sky and the antenna pattern, using only the position and time of observing of the input spectrum. This enabled us to generate stray profiles for positions and times that were never actually observed. Such simulations allowed us to study the behavior of the antenna under controlled circumstances, and led to some interesting results. Two figures illustrate the use of the correction procedure in “simulation mode”. Dummy profiles were given the relevant parameters for position and time, and were used as input spectra.

The upper panel of Fig. 10 shows the variability of the FSL component over a 24-hour (sidereal time) period. For $(l, b) = (160^\circ, +50^\circ)$, a FSL stray profile was calculated at every full hour in LST for the date 1 January, 1994. The

results are displayed as a surface plot viewed from two different angles. The intensity axis is not shown, because the perspective distorts its usefulness in determining absolute readings; instead, the extremes in the peak values are given in the figure caption.

A second view of the FSL variability is given by the lower panel in Fig. 10, where the seasonal effects are shown. Again, FSL corrections were calculated for $(l, b) = (160^\circ, +50^\circ)$, but this time the LST was kept constant at $6^{\text{h}}04^{\text{m}}$ (culmination of the source), while the date was varied in roughly 15-day steps. The FSL profiles reflect the varying LSR velocity correction necessitated by the Earth’s revolution around the Sun.

We note that the amplitude of the FSL correction amounts to a *full order of magnitude more* than the rms noise in the HI spectra in the survey. We note also that the large and varying widths of the FSL profiles provide an additional mandate for the correction. It seems worthwhile to stress this point by noting that even if a particular direction would have no HI whatsoever within the main beam, the uncorrected observations would have displayed HI intensities with the spectral characteristics indicated in Fig. 10.

4.1.3. Tuning the FSL antenna pattern parameters

Four positions at intermediate- and high latitudes were observed repeatedly during the entire observing run. They were selected on the basis of previous experience with FSL corrections for the Effelsberg telescope (Kalberla 1978). Their spectra are characterized by a low-intensity narrow profile rendering these directions particularly susceptible to FSL contamination; the substantial latitudes of these positions furthermore ensures that a broad swath of the galactic equator presents itself to the far sidelobes.

Table 2. Selected positions that were observed frequently to help tune the FSL pattern model. The positions were selected for their particular susceptibility to stray-radiation contamination by virtue of their of weak total intensity, kinematic narrowness, and higher latitude. Except for the LJM Hole field, the fields refer to the numbering of Kalberla (1978)

l	b	N	field
150°5	+53°0	1749	LJM Hole
160°0	+50°0	1570	4
90°0	+40°0	1318	8
132°5	+30°0	1440	26

Table 2 lists the galactic coordinates, the number of observations, and the source of the test positions shown as examples below. As many observations to these positions were made, the entire range of FSL contaminations for different hour angles and seasons is represented. Comparing the corrected observations with each other provides

a direct indication of the accuracy of the correction procedure. If the corrections were perfect, then all corrected spectra should be identical, within the uncertainty of the spectral noise.

There are two ways of comparing results. One is to calculate a mean over all corrected spectra, and examine the residuals. Another way is to compare corrected spectra that are most dissimilar. In either case, any discrepancies must be explained and, if possible, accounted for by an improved FSL pattern. Both methods are applied and analyzed in Sect. 4.3.

Example 1: $(90^\circ, +40^\circ)$. Two observations of the test position $(l, b) = (90^\circ, +40^\circ)$ are shown in Fig. 11. The uncorrected spectra are plotted in the upper panel of each pair; the calculated NSL and FSL contributions are shaded. The total amount of stray radiation (NSL + FSL) is also shown. The lower panel shows the corrected spectra and the total stray profiles. It is obvious that the NSL profile is almost identical for the two observations, and that the differences are dominated by the FSL contribution. Note, however, the presence of NSL stray radiation near $v_{\text{LSR}} = -115 \text{ km s}^{-1}$. It is received in the NSL pattern from the $\sim 1 \text{ K}$ feature that is present in the spectrum at the same velocity. Before stray-radiation correction, the June, 1990, spectrum contained a component near $v_{\text{LSR}} = -65 \text{ km s}^{-1}$ and the March, 1992, profile had an 0.5 K feature near $v_{\text{LSR}} = +70 \text{ km s}^{-1}$. Both are shown to be stray radiation, and have disappeared in the corrected spectra.

It is appropriate to discuss in some detail the manner in which the stray radiation originates in the far sidelobes. Figures 12 and 13 support this discussion. Each panel in these two figures displays stray spheres, representing the projection of the full $2\pi \text{ rad}^2$ of the HI sky that is above the horizon at the moment of observing. The center corresponds to the zenith ($El = 90^\circ$), and the edge to the horizon ($El = 0^\circ$). The position of the dot (the main beam) reflects the azimuth-elevation pointing coordinates of the observation, as given at the bottom. The white region around the main beam is the NSL pattern (radius 16°), which was calculated separately. In the shaded area, the FSL pattern receives radiation from the sky. (The stray spheres are projected such that the antenna-pattern features remain essentially constant in shape; this accounts for the relative distortion of the stray spheres.)

In the two frames of the bottom-left panel of Fig. 12, the galactic plane ($b = 0^\circ$), the NGP ($b = +90^\circ$), and the line $l = 180^\circ$ are marked. The greyscale bar represents the LSR velocity correction between the main beam (black: $\Delta v_{\text{LSR}} = 0 \text{ km s}^{-1}$), and the other sky directions.

The top-left panel shows the stray spheres of the convolution of the HI sky brightness with the FSL antenna pattern, integrated over $[-250, +250] \text{ km s}^{-1}$ (the full range over which the stray-radiation contamination was calculated). Brighter pixels correspond to higher cross

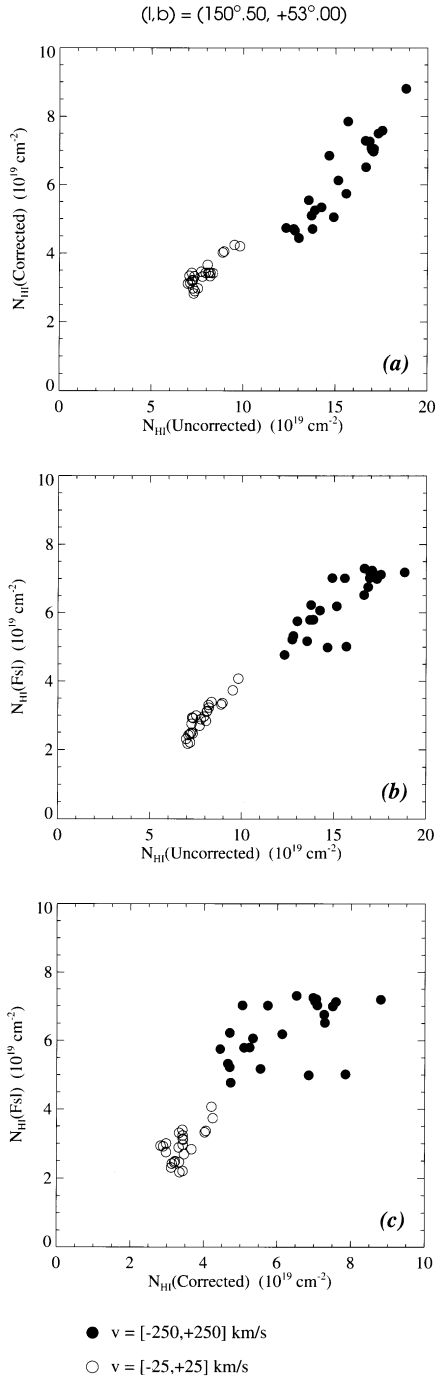


Fig. 21. Scatter diagrams of column densities derived from observed spectra, stray-radiation corrected spectra, and FSL contributions. **a)** Column densities from corrected spectra are correlated with those from uncorrected profiles. Perfectly corrected spectra should be scattered around a line of constant $N_{\text{HI}}(\text{corrected})$. **b)** Column densities in the uncorrected spectra are linearly dependent on the amount of FSL stray radiation (expressed as equivalent column density). **c)** $N_{\text{HI}}(\text{corrected})$ depends on the FSL contribution that was subtracted, indicating that FSL stray radiation is still present in the corrected profiles

sections. Clearly visible are the main components of the FSL pattern (spillover ring, stray cones, and leg shadows), especially where they intersect the galactic plane. The total integrated intensities are indicated by Σ , which represents N_{HI} in units of K km s^{-1} .

The six panels of stray-sphere pairs on the right show how the FSL radiation is distributed over different velocity intervals. The scaling is relative to the total integrals; integrated intensities over the indicated velocity intervals are given.

The individual frames enable detailed analysis of the origin of the spectral components caused by the FSL contamination. The component near $v_{\text{LSR}} = -60 \text{ km s}^{-1}$ (Fig. 11a), is seen in both the $[-200, -60] \text{ km s}^{-1}$ and the $[-60, -20] \text{ km s}^{-1}$ stray spheres, and is mainly caused by galactic-plane gas emitting into the stray cones. The Δv_{LSR} sphere shows that the velocity shift is negative in that area, but not as large as -60 km s^{-1} . That implies that the component originates from (negative) intermediate-velocity gas that is shifted to more negative values.

The FSL component near $v_{\text{LSR}} = +70 \text{ km s}^{-1}$ seen in Fig. 11b is clearly present in the $[+60, +200] \text{ km s}^{-1}$ frame. It has the highest FSL contribution ($\Sigma = 11.2 \text{ K km s}^{-1}$) of all frames shown. The bright regions are identified with the spillover ring; the cross section is highest where this ring overlays the galactic plane. In that region, the Δv_{LSR} is about $+70 \text{ km s}^{-1}$, which implies that the (high intensity) galactic-plane emission near zero velocity is directly shifted to the velocity of the FSL emission feature.

Both observations shown in Fig. 11 were made at roughly the same azimuth and elevation, but in different seasons. The orientation of the galactic plane with respect to the FSL pattern is quite similar, but the LSR velocity correction has changed due to the different location of the Earth in its orbit around the Sun.

Example II: (160°, +50°). Another illustration of the details of the stray radiation entering the FSL antenna pattern is shown by the observations in Figs. 13 and 14. In this example, the pointing of the telescope was quite different for the two observations of $(l, b) = (160^\circ, +50^\circ)$; this difference is directly reflected in the stray spheres. The high-elevation (73°) of the November, 1990, observation places the main beam near the zenith, and projects the four stray cones entirely onto the sky. The spillover ring, however, is completely on the ground. For the June, 1992, observation, half of the spillover, and only two of the stray cones, are directed towards the sky. Also, the orientation of the galactic plane is distinctly different in the two cases.

Figure 14a shows a prominent FSL component of about 0.5 K peak intensity, near $v_{\text{LSR}} = +25 \text{ km s}^{-1}$. The stray spheres at $[0, +20] \text{ km s}^{-1}$ and $[+20, +60] \text{ km s}^{-1}$ reveal that the galactic plane is received in the stray cones,

at a moderately positive velocity. The contribution from these velocity intervals is 65% of the total FSL component.

Quite the opposite situation is displayed in Fig. 14b. Very prominent FSL stray radiation is seen near $v_{\text{LSR}} = -40 \text{ km s}^{-1}$, reaching a peak intensity of about 0.7 K. From the stray spheres, it is clear that 56% of the total stray radiation is received in the interval $[-60, -20] \text{ km s}^{-1}$. The major contribution comes from the spillover ring, especially where it overlays the galactic plane. The LSR velocity correction agrees with the assumption that the zero-velocity HI gas from the galactic plane is shifted by this amount, and is received in the spillover ring. These examples demonstrate the following characteristics of the FSL stray-radiation contribution:

1. The total integrated intensity received in the FSL antenna pattern is highly variable. In Fig. 14b, it is 40% higher than in Fig. 14a.
2. The velocity distribution of the FSL radiation depends mostly on how the $v_{\text{LSR}} \sim 0 \text{ km s}^{-1}$ emission from near the galactic plane is shifted with respect to the main beam.
3. The elevation of the observation determines whether sensitive parts of the FSL pattern are “up” or “down”. In Fig. 14a, the spillover ring is fully on the ground, and thus does not receive sky emission.

The two examples shown in the paragraphs above give results from the optimized FSL pattern. Using displays like Figs. 12 and 13, the source of the FSL components can be identified. If a feature was present in one spectrum, and not in another, it was assumed to be FSL stray radiation. If it had not disappeared after the correction, displays like the ones shown here were used as diagnostics to optimize the FSL pattern.

The complicated interplay between FSL sensitivity, sky brightness, and velocity shift, makes it quite difficult to trace the exact origin of stray components. For example, comparing the lower panels in Figs. 14a and 14b, it is obvious that there is additional emission near $v_{\text{LSR}} = -40 \text{ km s}^{-1}$ in the June, 1990, observation. This implies that either the Fig. 14a spectrum was over-corrected, because it shows less emission, or that the Fig. 14b spectrum was not corrected enough. In either case, the difference indicates the *worst-case* limitation to our procedure. The prime precaution in the FSL correction algorithm, was to guard against over-corrections. A too-high estimate of the FSL contribution would create an interval of negative intensity in the spectrum upon subtraction. Such intervals are unacceptable, but easily detected.

When it was suspected that a component was insufficiently corrected, the analysis proceeded approximately as follows. Suppose the $\sim 0.25 \text{ K}$ component near $v_{\text{LSR}} = -40 \text{ km s}^{-1}$ in Fig. 14b must be accounted for in the FSL calculation. Assuming it was caused by the $v_{\text{LSR}} = 0 \text{ km s}^{-1}$ component near the galactic plane, shifted by -40 km s^{-1} ,

we can identify the regions where $b = 0^\circ$ acquires the appropriate velocity shift. As it turns out in this case (see the velocity-shift illustration of Fig. 13b), the velocity gradient is almost perpendicular to lines of constant latitude. That makes it difficult to identify the FSL region that was underestimated. The complications become greater when a new component has to be considered, rather than assuming that a known component was underestimated. Also, the assumption that the component is caused by gas near zero velocity does not always hold true.

Despite these difficulties, it proved possible to tune the known features in the FSL pattern with the aid of many examples at identical positions, observed under widely varying circumstances. We address the search for a possible additional FSL component in Sect. 4.3.

4.2. Near-sidelobe corrections

The NSL pattern was defined as covering the region $0^\circ \leq \theta \leq 16^\circ$; it represents only 0.5% of the entire antenna pattern. Nevertheless, half of the total stray-pattern sensitivity is contained in this solid angle. The NSL contribution is almost constant with time, mainly because the pattern is highly symmetrical, and will therefore not yield a different convolution when the input sky is rotated with respect to the main beam. The NSL contribution largely mimics the shape of the spectrum in question. Thus, although correct recognition of the NSL contribution is crucial to an accurate determination of total column depths or of peak brightness temperatures, the near sidelobes do not introduce spurious additional spectral components in the manner of the far sidelobes. The NSL contamination generally broadens spectral features.

The combined MB + NSL region of the antenna pattern can be regarded as the point-spread function of the telescope. Therefore, the effect of correcting a spectrum for the NSL stray-radiation contamination is, in principle, a deconvolution to a pencil-beam (main beam) response. The net result of the NSL corrections are sharper images.

The examples in Figs. 11 and 14 show that the NSL contribution is more or less constant with time, and that for intermediate $|b|$, some 50% of the total stray radiation is contained in the NSL profile. The situation is different near the galactic plane; there, the intensities are high, and so the NSL pattern receives more power than at high $|b|$. Figure 15 shows a spectrum in the galactic plane, at $(l, b) = (20^\circ, 0^\circ)$, together with the stray-radiation contributions. In the full-scale plot of the uncorrected spectrum (top), the NSL profile is seen to be responsible for about 15% of the total emission received. The central panel shows that the FSL contribution is insignificant.

An example of NSL stray radiation near the galactic center is shown in Fig. 16. At $(l, b) = (1^\circ, 0^\circ)$, strong absorption is visible at $v_{\text{LSR}} = 6 \text{ km s}^{-1}$, because the HI absorption signature associated with local molecular material is quite extended on the sky. This component is

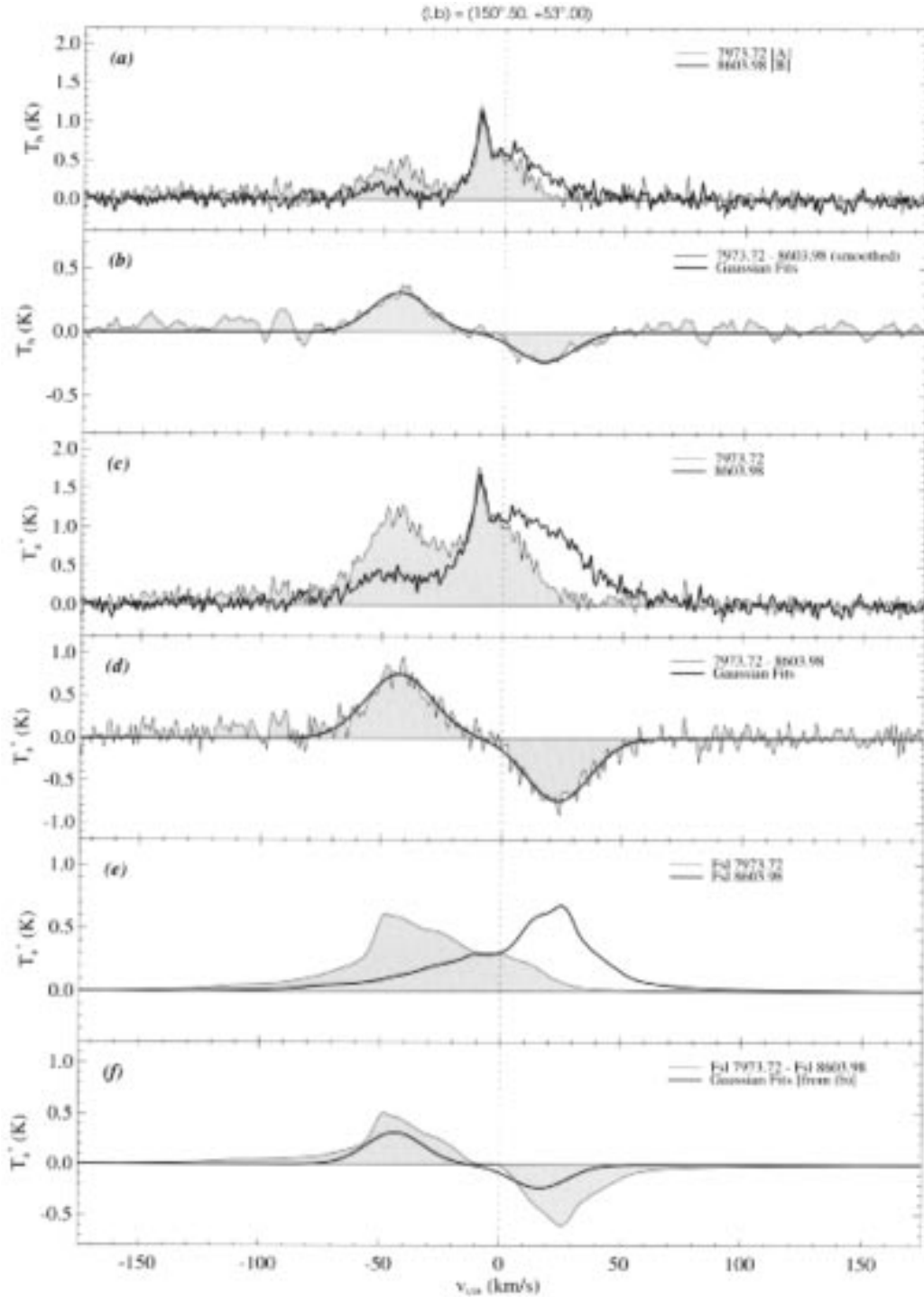


Fig. 22. Two dissimilar observations of the LJM Hole. The spectra (indicated with [A] and [B]) were taken from the test suite shown in Fig. 19. **a)** Corrected profiles are distinctly different, although the peak temperatures are equal. **b)** Difference spectrum of the corrected profiles. The anti-symmetric residuals can be fitted by two Gaussian distributions. The components of the fit are given in the text. **c)** Spectra as observed, with no stray-radiation corrections applied. **d)** Difference profile from **c)**, providing a minimal estimate of the stray radiation. Equal contributions have cancelled, but the unique FSL contamination in each spectrum is seen as a residual component. The Gaussian fits are anti-symmetric, and contain equal amounts of equivalent column density. **e)** Calculated FSL profiles, showing almost perfect mirror images. **f)** Difference spectrum of the FSL contributions, exhibiting the same characteristic shape as the Gaussian fits from **b)**. This similarity suggests that the residuals in **b)** are also FSL stray radiation. The possible origin of this additional FSL component is discussed in the text

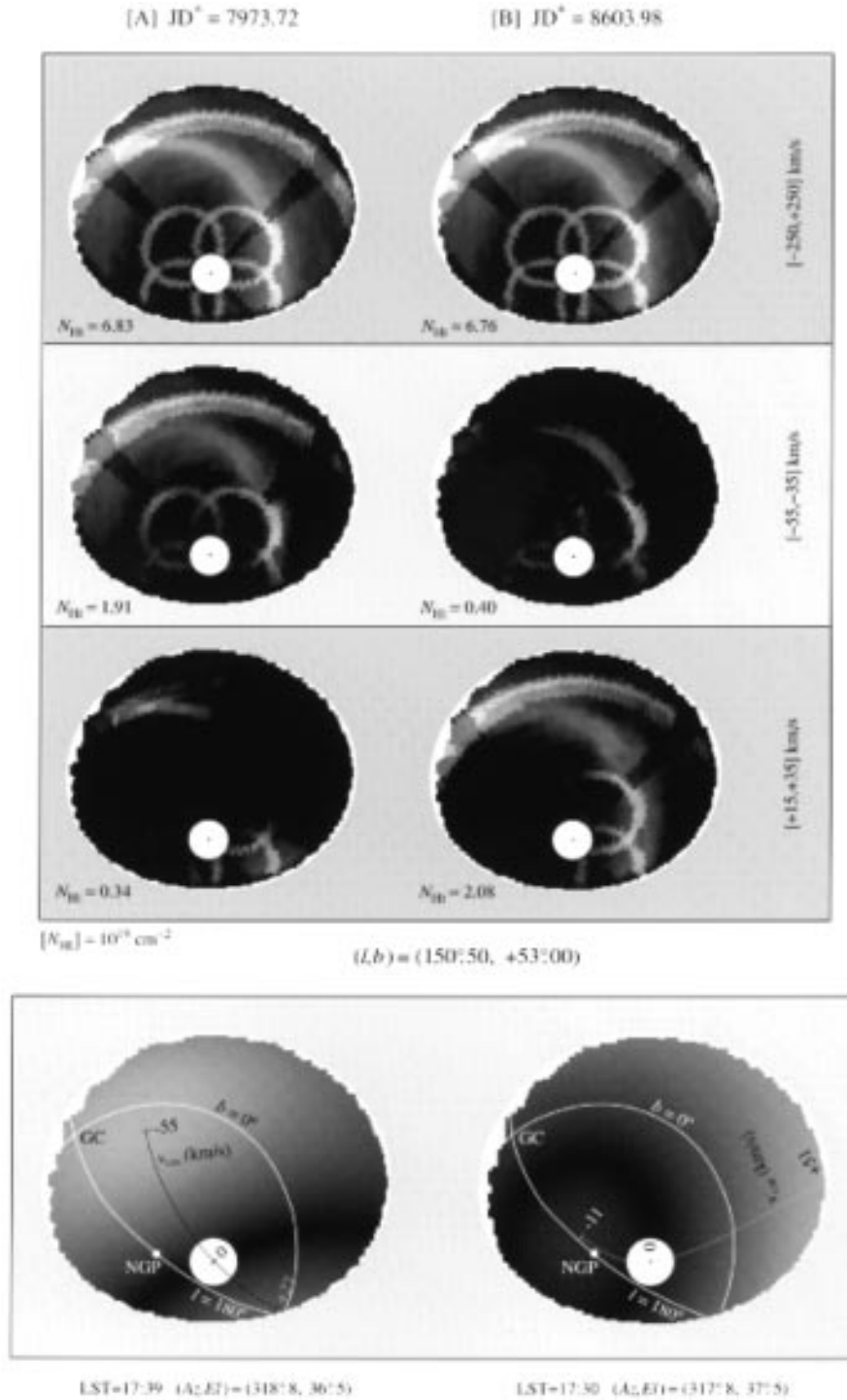


Fig. 23. Stray spheres for the two observations toward the LJM Hole shown in Fig. 22. (A description of the general features of these panels is given in the caption of Fig. 12.) The FSL contributions integrated over the entire velocity range entering the calculations (shown in the uppermost panel) are virtually identical. The remaining two upper panels indicate how the stray radiation is distributed over the sky for velocity intervals centered on the peaks of the observed far-sidelobe residuals (see Fig. 22d). The bottom panel shows that the observing conditions were almost identical when the two spectra were taken. Both the telescope pointing and the orientation of the galactic plane with respect to the main beam (and the FSL pattern) were similar. Only the season of observing was different, yielding different LSR velocity gradients. The far sidelobes receive equal amounts of emission near zero velocity, mainly from the galactic plane, but shifted to opposite velocities. This explains the anti-symmetry which is seen in Fig. 22e

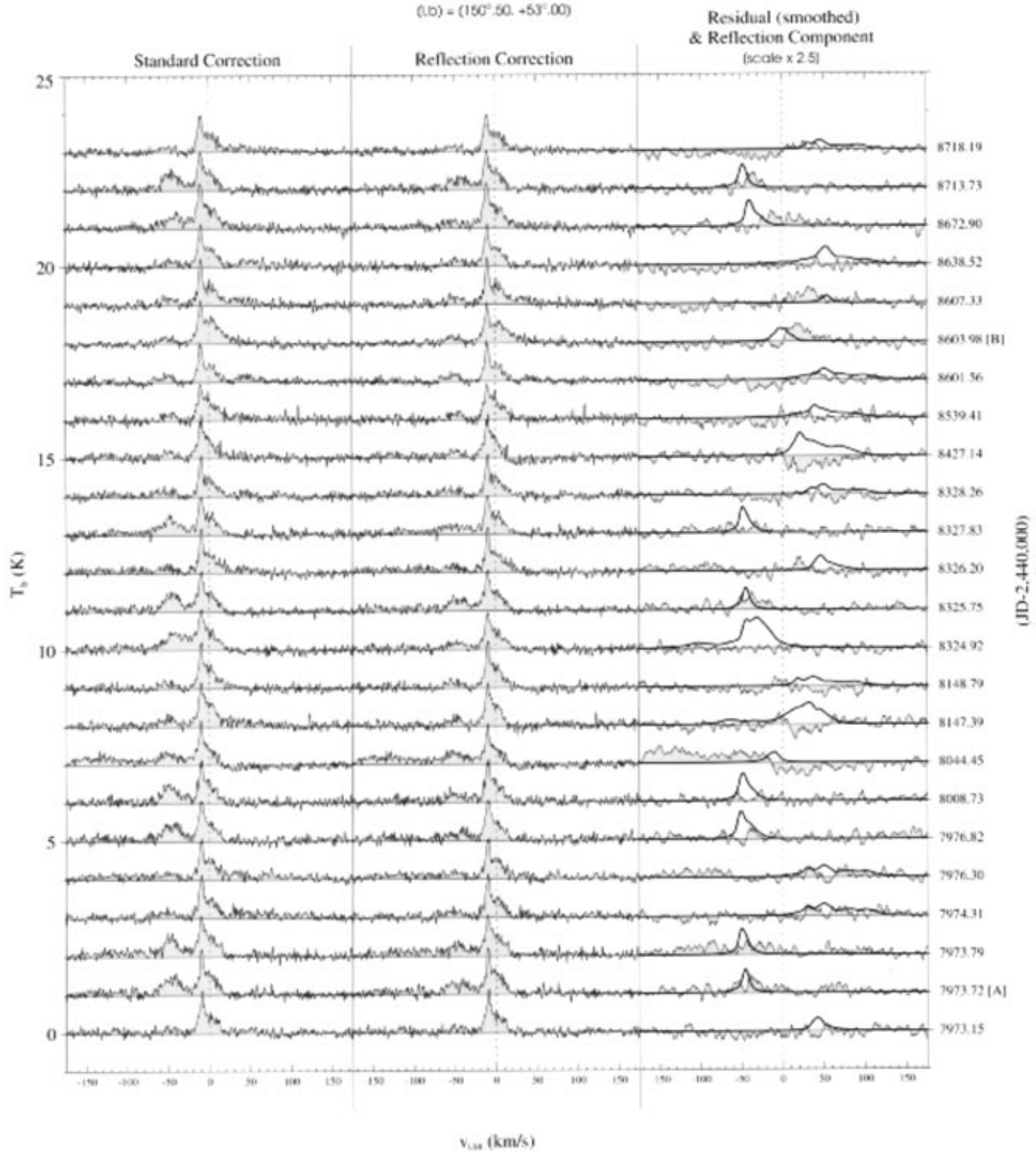


Fig. 24. Spectra from the test suite of 24 observations towards the direction of the LJM Hole region. The standard stray-radiation (NSL + FSL) corrected spectra (left) are compared with corrected profiles to which an additional reflection correction was applied (center). The residuals (right; shaded) were obtained by subtracting the mean of the reflection-corrected profiles. The individual reflection components are superimposed (right; heavy line). Note the magnified scaling of profiles in the right column. Prominent reflection was successfully subtracted, for example, from $JD^* = 8324.92$, while the correction for $JD^* = 8427.14$ was less satisfactory. The spectra labeled [A] and [B] are considered in more detail in Fig. 25 and in the accompanying discussion in the text

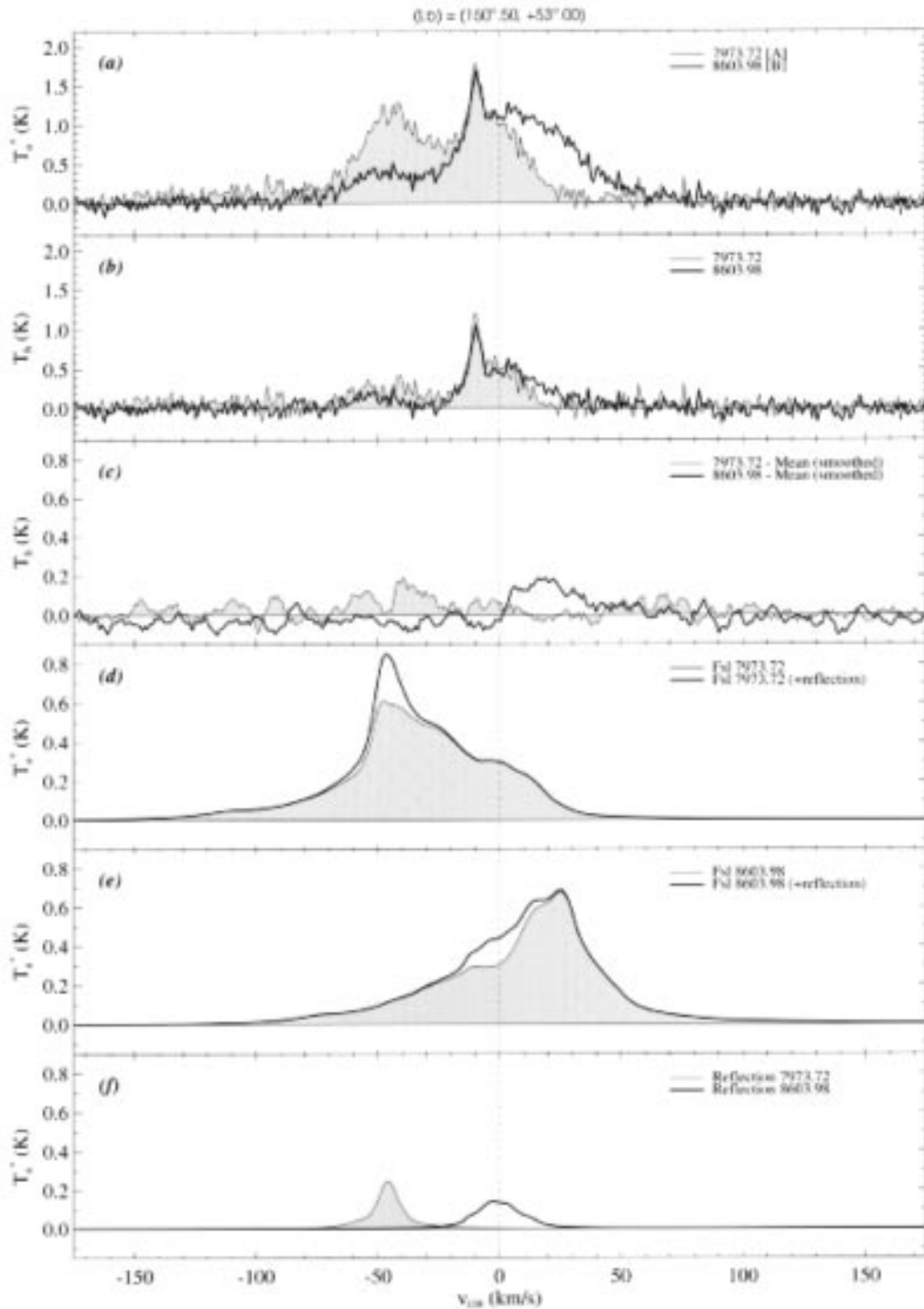


Fig. 25. Two dissimilar spectra (indicated with [A] and [B]) taken from the test suite of observations towards the direction of the LJM Hole region. **a)** Uncorrected profiles show large differences. **b)** Spectra after correction for NSL, FSL, and RSL contamination are in better agreement (cf. Fig. 22a). **c)** Residuals of the corrected spectra shown in **b)** after subtraction of the mean of all 24 corrected profiles in the test suite. Comparison of the FSL stray radiation (shaded) with the FSL + RSL calculations (heavy line) for [A] and [B] are shown in **d)** and **e)**, respectively. **f)** Individual RSL components calculated for [A] and [B]

also present in the NSL profile. After subtraction of the stray radiation, the absorption is more prominent.

4.3. Observations of the LJM Hole

The region in Ursa Major centered roughly on $(\alpha, \delta)_{1950} = (10^{\text{h}}42^{\text{m}}, +58^{\circ})$ was called “The Hole” by LJM, because it has the lowest HI column density known on the sky. Specifically, towards $(l, b) = (150^{\circ}5, +53^{\circ}0)$, the mean N_{HI} was reported to be $5.9 \cdot 10^{19} \text{ cm}^{-2}$. In a later paper by Jahoda et al. (1990), the weakest galactic 21-cm line was found in the direction $(\alpha, \delta)_{1950} = (10^{\text{h}}36^{\text{m}}58^{\text{s}}, +57^{\circ}20'00'')$, with an $N_{\text{HI}} = 4.4 \cdot 10^{19} \text{ cm}^{-2}$. Their spectrum (reproduced in Fig. 17) was observed with the NRAO 140-ft telescope, and was corrected for stray radiation in the manner described by LJM (see also Sect. 1.3). The irregular baseline is a consequence of the correction procedure. The spectrum from the Leiden/Dwingeloo survey with position nearest that of the Jahoda et al. profile is shown in Fig. 18. Despite the different telescopes and receiver systems, the somewhat different pointing directions, and the different approaches to the stray-radiation correction, the two spectra are satisfyingly similar.

4.3.1. Repeated observations of the LJM hole

The conditions for stray-radiation contamination are particularly unfavorable for the Hole region. Not only is the column density the lowest on the sky, but also the high galactic latitude allows the galactic plane to be received in large cross sections with the FSL pattern (see Fig. 23). As mentioned above, frequent observations were made towards $(l, b) = (150^{\circ}5, +53^{\circ}0)$. A test suite of 24 observations of this position, used to tune the FSL pattern, is shown in Fig. 19. The observed profiles are plotted together with the corrected spectra. The residuals resulting from subtraction of the mean corrected profile are also given. The results indicate the approximate accuracy of the correction procedure. The results also suggest the possible existence of an unaccounted-for component. In the discussion below, we tentatively identify this component with 21-cm radiation reflected from the ground and vegetation near the telescope.

The corrected profiles in Fig. 19 show no sign of over-correction, that is, they show no negative-intensity intervals in the baseline as a result of subtracting a too-high estimate of the stray radiation. It is thus plausible that some spectra have not been corrected enough, giving rise to left-over stray radiation. Such residuals would be present in the mean corrected spectrum, yielding the negative residuals seen in some cases.

As stated above, the NSL contribution to the stray radiation at a given direction hardly varies with time. In this sample of 24 spectra, the average equivalent column density due to the NSL contribution was $2.82 \pm 0.009 \cdot 10^{19} \text{ cm}^{-2}$, which amounts to an 0.3% variation.

The behavior of the FSL stray radiation is shown in Fig. 21. The column densities of the observed and the corrected spectra, and the equivalent FSL column densities, integrated over a narrow- and a broad- velocity interval, are represented in scatter diagrams. Figure 21a shows that the column density of a corrected profile is still correlated with N_{HI} of the observed spectrum. Perfectly corrected spectra would be seen scattered around a line of constant N_{HI} (corrected). The N_{HI} (FSL) shows the same dependency with N_{HI} (uncorrected). This is, of course, expected: the excess equivalent N_{HI} in the uncorrected profiles is attributed to FSL stray radiation (disregarding the constant NSL radiation). Nevertheless, panel (a) in Fig. 21 shows that the calculated correction was not always sufficient. Although the scatter is somewhat larger in panel (c), this plot proves that the N_{HI} (corrected)– N_{HI} (uncorrected) dependency is not due to a general scaling problem. If the spectra in the test suite were inhomogeneously scaled, the linear dependency as in panel (a) would be the result. However, panel (c) shows that N_{HI} (corrected) remains dependent on N_{HI} (FSL). This implies that the FSL stray radiation is insufficiently removed, leaving the corrected profiles still containing a weak FSL component.

Figure 20 shows details of the stray-radiation contamination of two spectra from the test suite. The profile shown in panel (a) of the figure was observed at $\text{JD}^* = 7973.15$ ($\text{JD}^* = \text{JD} - 2,440,000$). The combined NSL + FSL stray radiation covers the extended shoulders of the observed spectrum. After subtraction there appears to be no significant emission for $|v_{\text{LSR}}| > 25 \text{ km s}^{-1}$ in the corrected profile. The example shown in Fig. 20b was observed at $\text{JD}^* = 7973.72$ (that is, only $13^{\text{h}}40^{\text{m}}$ after the spectrum in panel (a)), and contains a considerable residual component near $v_{\text{LSR}} = -50 \text{ km s}^{-1}$. The corrected spectrum appears identical to the one in panel (a), for $v_{\text{LSR}} \geq -25 \text{ km s}^{-1}$. The crucial question is therefore: is the -50 km s^{-1} component real (and was it erroneously removed from the profile in panel (a)), or is it spurious, contributed by inadequately accounted-for stray radiation?

4.3.2. Interpreting residuals

We argued above that in some cases stray radiation may have been insufficiently removed. The spectra in the test suite are about one Dwingeloo beamwidth away from the position with the lowest column density on the sky (see Figs. 17 and 18). The profiles at the two positions are quite similar; the component near -50 km s^{-1} is prominently present both in the 140-ft and in the 25-m spectra. This challenges the previous assumption that this component, when seen in spectra one beamwidth away, is FSL stray radiation. If it is real, then the profile in Fig. 20a is over-corrected. Otherwise, the 140-ft telescope has suffered from similar unaccounted-for stray radiation.

A detailed look at the individual 140-ft observations of the Hole and their respective corrections might provide a better insight into this problem.

It remains curious that, if the -50 km s^{-1} component is real, N_{HI} in the corrected profiles is still correlated with the $N_{\text{HI}}(\text{FSL})$. Figure 20b demonstrates that this is particularly true for the spectral distribution of the FSL radiation, which is lopsided, and peaks at the -50 km s^{-1} feature. In the absence of the feature, as in the corrected spectrum of Fig. 20a, the FSL profile has no apparent peak.

Another approach to understanding the inconsistencies in the corrected spectra involves comparing profiles that are most prominently dissimilar. Figure 22 shows a detailed analysis of two spectra from the test suite (labeled [A] at $\text{JD}^* = 7973.72$ in Fig. 20 and [B] at $\text{JD}^* = 8603.98$) that appear very different before stray radiation correction.

The *observed* profiles are shown in Fig. 22c; in panel (d) the difference spectrum is plotted. Remarkably, the difference spectrum is quite symmetrical, and can be fitted well by two Gaussian distributions with the following parameters:

spectrum	v_{LSR} (km s^{-1})	σ_v (km s^{-1})	T_{max} (K)	N_{HI} (cm^{-2})
A(uncor.)	-42	17	0.75	$4.7 \cdot 10^{19}$
B(uncor.)	+24	16	-0.74	$-4.4 \cdot 10^{19}$

The anti-symmetry with respect to $v_{\text{LSR}} = 0 \text{ km s}^{-1}$ is evident in the values of N_{HI} , T_{max} , and σ_v . The deviation from symmetry for the central velocity of the Gaussian distributions is -18 km s^{-1} , which is about equal to the component of the Standard Solar Motion used in the LSR correction.

The *corrected* profiles and their difference spectrum are plotted in panels (a) and (b), respectively, of Fig. 22. Again, two Gaussian distributions serve to model the differences well:

spectrum	v_{LSR} (km s^{-1})	σ_v (km s^{-1})	T_{max} (K)	N_{HI} (cm^{-2})
A(corrected)	-43	14	0.31	$1.7 \cdot 10^{19}$
B(corrected)	+17	14	-0.23	$-1.2 \cdot 10^{19}$

The similarity between the Gaussian fits of the difference spectra before and after correction suggests that they represent the same component, namely the FSL stray radiation. Figure 22a displays the calculated FSL components, and panel (f) the difference profile, with the Gaussian fits from panel (b) overlaid. The same symmetry is observed, and the residuals in the corrected spectra (represented by the Gaussian fits) correlate quite well, especially at negative velocities. The implication that the residuals are due to yet-unaccounted-for FSL stray radiation is, again, quite strong.

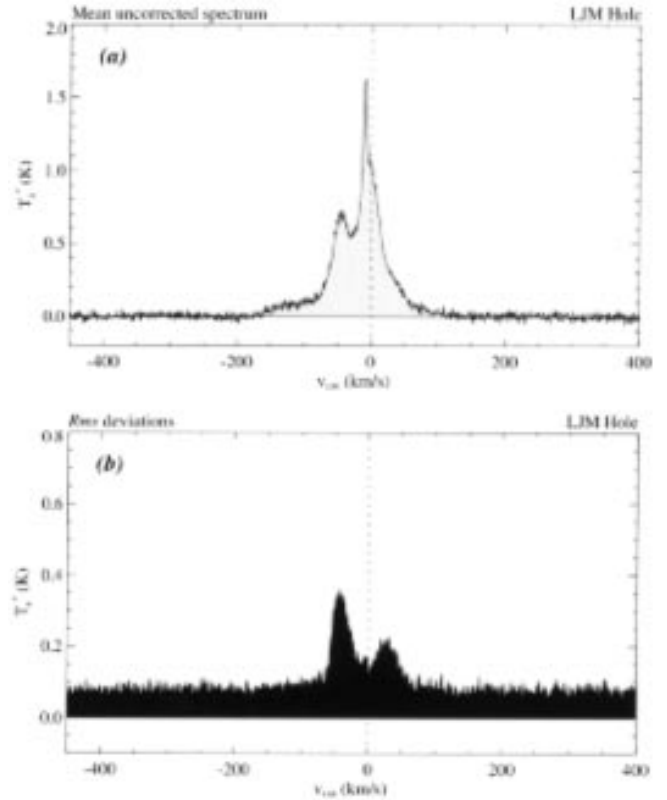


Fig. 26. **a)** Mean spectrum of the uncorrected profiles in the test suite of observations towards the LJM Hole. **b)** Channel-by-channel rms deviations of the individual spectra from the mean spectrum shown in **a)**. The mean level outside the velocity range for which stray radiation was calculated are indicative of the spectral noise due to the receiver system and the reduction procedure. Without stray-radiation correction the uncertainties for $|v_{\text{LSR}}| < 100 \text{ km s}^{-1}$ in the spectral intensities of spectra of low column density exceed the rms spectral noise due to the receiver system and the reduction procedure by an order of magnitude

4.3.3. Consulting the stray spheres

To analyze the details of the FSL correction, Fig. 23 shows the appropriate stray spheres, similar to those presented in Figs. 12 and 13. The integration intervals were chosen to encompass the residual components in the uncorrected difference spectrum (Fig. 22b). The bottom panel of Fig. 23 shows that the observing conditions for the two spectra were nearly identical. The telescope pointing and the orientation of the galactic plane with respect to the main beam were the same. The only distinguishing factor was the season of observing, and therefore the direction of the LSR velocity gradients, which are seen to be almost perpendicular to each other. The total integrated FSL contributions, shown in the upper panel, are identical both in column density as well as in sky distribution. The velocity distribution is, however, clearly asymmetrical, as can be seen in Fig. 22e. The stray spheres corresponding to the

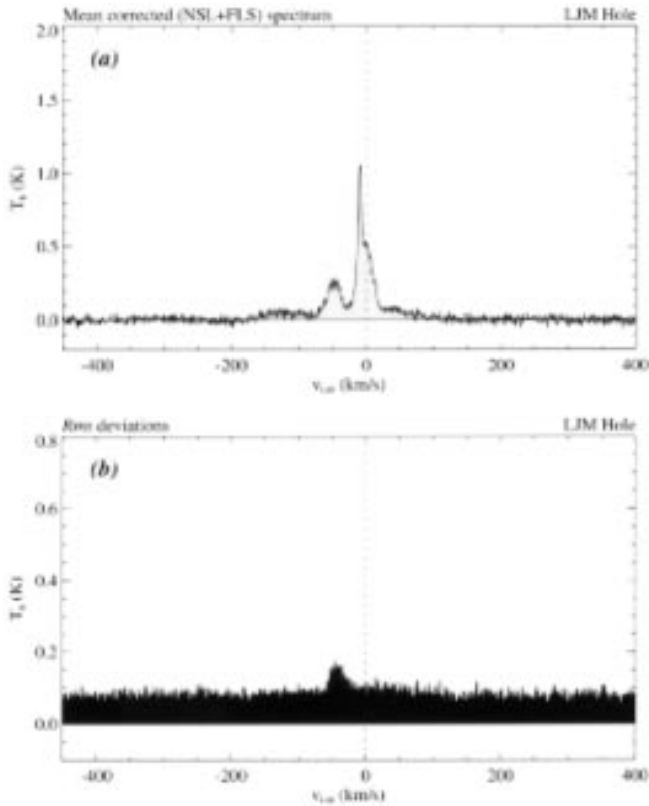


Fig. 27. a) Mean spectrum of the stray-radiation (NSL + FSL) corrected profiles in the test suite of observations towards the LJM Hole. **b)** Channel-by-channel rms deviations of the individual spectra from the mean spectrum shown in **a)**. The stray-radiation correction greatly reduces the uncertainties in the spectra for $|v_{\text{LSR}}| < 100 \text{ km s}^{-1}$ (cf. Fig. 26b). The mean discrepancies over this velocity interval are of the order of the rms spectral noise due to the receiver system and the reduction procedure. These data refer to a single direction and thus do not provide a general estimate of the accuracy of the correction procedure

indicated velocity intervals reveal that the largest cross sections originate from different regions of the sky. Nevertheless, the FSL profiles are strongly anti-symmetric. It is therefore expected that an unaccounted-for FSL feature will give rise to residuals that are likewise anti-symmetric with respect to $v_{\text{LSR}} = 0 \text{ km s}^{-1}$. Since this is precisely what is seen in Fig. 22b, it seems plausible that some FSL stray-radiation is, indeed, still present and contaminating the corrected spectra.

The above line of argument also suggests that the component near $v_{\text{LSR}} = -50 \text{ km s}^{-1}$ in the spectrum observed on $\text{JD}^* = 7973.72$ is most likely FSL stray radiation. We do note, however, that such a situation implies that the 140-ft spectrum, which contains this very same component, is likewise affected by additional stray radiation. (Unfortunately, no direct comparison could be made with the data published by Willacy et al. (1993). Although

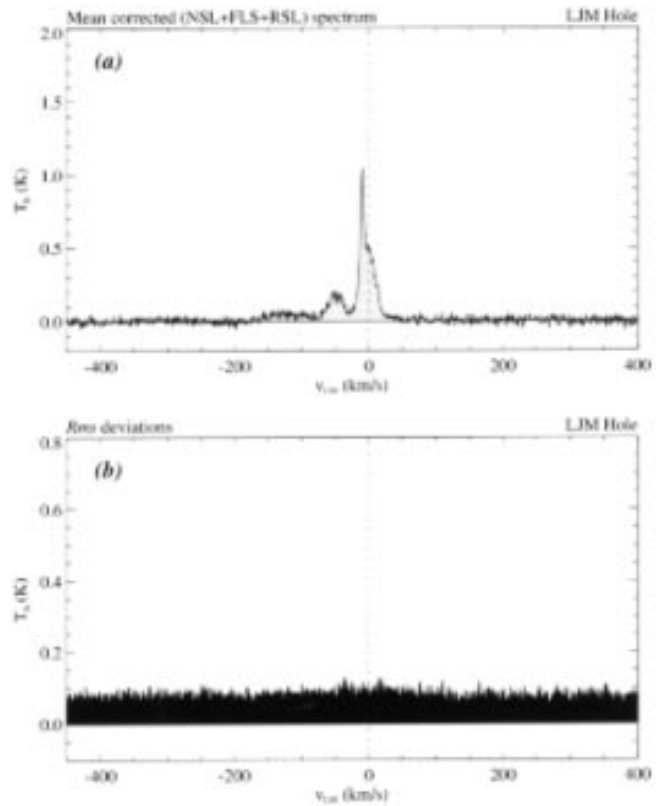


Fig. 28. a) Mean spectrum of the stray-radiation (NSL + FSL + RSL) corrected profiles in the test suite of observations towards the LJM Hole. **b)** Channel-by-channel rms deviations of the individual spectra from the mean spectrum shown in **a)**. With the application of the RSL correction, uncertainties for $|v_{\text{LSR}}| < 100 \text{ km s}^{-1}$ disappear in the general rms noise due to the receiver system and the reduction procedure (cf. Fig. 27b). We note that the reflection correction procedure was tuned using the spectra in this test suite; the accuracy of this method may not be derived from the rms values shown in **b)**

these authors plotted the spectra observed around the Hole, the size of the published profiles ($3 \times 1.5 \text{ mm}$) was too small to allow any comparison with the Leiden/Dwingeloo data.)

4.3.4. Incompleteness of the input sky

The stray spheres shown in Fig. 23 are not as smooth as those shown in Figs. 12 and 13. The jagged edge on the horizon is caused by the incompleteness of the input sky. Although the Leiden/Dwingeloo survey encompasses the complete sky accessible from Dwingeloo, the sky that never rises above $3^\circ 5'$ elevation (the physical limit of the telescope) could not be reached by the main beam. The FSL pattern did, nevertheless, receive emission from those regions. This could be of some influence on the FSL correction, when sensitive areas in the FSL pattern point to parts of the galactic plane at inaccessibly-low

elevations. The lower panel in Fig. 23 shows that this situation occurred for the present examples, as the galactic plane just beyond the galactic center coincides with part of the spillover ring. The $v_{\text{LSR}} = 0 \text{ km s}^{-1}$ emission from that region was shifted to about $v_{\text{LSR}} = -40 \text{ km s}^{-1}$ in (A), and to about $v_{\text{LSR}} = +15 \text{ km s}^{-1}$ in (B). This agrees well with the residual components at $v_{\text{LSR}} = -43 \text{ km s}^{-1}$ (A) and $v_{\text{LSR}} = +17 \text{ km s}^{-1}$ (B) in Fig. 22d.

To further confront the suspicion that the very low-elevation sky could distort the data, we filled the empty regions in the sky model by mirroring the observed sky cells at $l \geq 0^\circ$ in the line $l = 0^\circ$. This first-order estimate of the galactic plane at $l < 360^\circ$ seemed quite acceptable, but did not resolve the problem. The cross sections between the newly create sky elements and the spillover ring were not sufficient to remove the residual components.

4.3.5. Possible reflections off the local terrain

We mentioned earlier (Sect. 2.2) that the Moon has an estimated albedo of 0.07 for the 21-cm line. HI emission reflected off the Moon could be clearly identified as such. We considered whether additional sources of reflected radiation might be relevant.

A body of water seen close to glancing incidence is an effective flat mirror to radio waves. This was demonstrated by one of the earliest radio interferometers, which used the signal reflected by the sea as a second path between a source and the receiver (Bolton & Stanley 1948). We note that the Dwingeloo telescope is located at the edge of an extensive, very flat, largely tree-less heath. That landscape affords distant horizons, and is frequently very wet.

Little is known about the HI reflectivity of soil and vegetation. Extended studies exist on the subject of back-scattering of radar from a great variety of natural objects (employed in the field of remote sensing). Some radar bands are quite close to 1420 MHz, and these data provide a few useful leads. Radar at decimeter wavelengths is back-scattered from all sorts of natural objects (grass, trees, scrubs, etc.). It therefore seems likely that it can be reflected in the forward direction as well. The reflectivity is strongly dependent on the moisture content and physical appearance of the scattering objects. For example, dry grass, wet grass, snow-covered grass, and ice-covered grass all reflect radar waves differently.

The Dwingeloo telescope is situated on the border (directed roughly east-west) between a forest (to the north) and a heath (to the south). The heath stretches unobstructed for many kilometers, and contains some small pools of water. The weather while observing might well be an important influence on 21-cm reflectivity. The season may also be of influence, because it determines the overall condition (size, moisture, etc.) of the vegetation and the soil. Since none of this information is available for the survey data, we experimented with models based

on some crude assumptions, and reached some speculative conclusions.

We explored the Dwingeloo heath south of the telescope and sketched a map paying particular attention to the location of various pools and ponds. The model for ground reflection was based on these sketches. Because of our lack of knowledge on the mean reflectivity of the ground, the initial modeling attempts were made with a 100% reflectivity, in order to study the effects of reflection on the total FSL contribution into the extreme. Although generally over-correcting the profiles, it did account for some of the features that were considered left-over stray radiation. The final, though still crude, model we tested contained a parameterization of the terrain to the south of the telescope, as given in Table 3. We call the reflection profiles calculated with this model the *reflection sidelobes*, or RSL for short. The assumed reflectivities, α , are extremely high (cf. 0.07 for the Moon), but the results of this empirical model are nevertheless evidently useful.

Table 3. Parameters of the ground-reflection model. The range in azimuth covers the terrain to the south of the telescope. Estimates for the reflectivity, α , and the maximum reflection angle, β_{max} , are given

Az	El	α	β_{max}
110°	0°	0.0	30°
120°	0°	0.5	30°
130°	0°	0.5	40°
140°	0°	0.5	50°
150°	0°	0.5	80°
160°	0°	0.5	80°
170°	0°	0.5	70°
180°	0°	0.8	70°
190°	0°	1.0	80°
200°	0°	1.0	80°
210°	0°	1.0	80°
220°	0°	1.0	70°
230°	0°	0.8	70°
240°	0°	0.8	60°
250°	0°	0.5	50°
260°	0°	0.0	20°

In Fig. 24, the results of the ground-reflection calculations are compared with the results from the regular stray-radiation correction (NSL + FSL) for the test suite of observations of the LJM Hole. The profiles on the left are the corrected profiles from Fig. 19. The center column shows the profiles after additional subtraction of the calculated RSL component. Most residual components have been reduced considerably, without affecting the baseline. The only exception seems to be the spectrum observed on $\text{JD}^* = 8427.14$. On the right, the residuals after subtraction of the mean are plotted with the RSL component superimposed. The scale is magnified by a factor of 2.5 to enhance the details. The majority of the RSL profiles

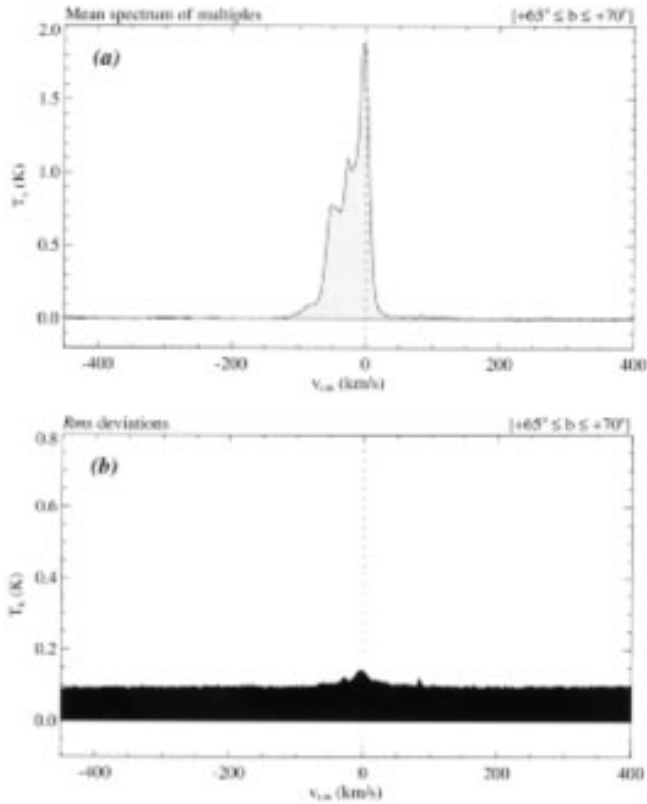


Fig. 29. **a)** Mean of the averaged multiply-observed spectra in the latitude strip $65^\circ \leq b \leq 70^\circ$. The spectrum has little astrophysical relevance (but it does show the generally low spectral intensities at high latitudes). **b)** Mean of the channel-by-channel rms deviations of the individual (multiply-observed) spectra from their averaged profiles. The deviations for $|v_{LSR}| < 100 \text{ km s}^{-1}$ are mainly due to uncertainties in the FSL stray-radiation corrections. No RSL correction was attempted for these spectra. The accuracy of the stray-radiation correction procedure is estimated from these data; they are representative for the entire observing period. The average uncertainties for $|v_{LSR}| < 100 \text{ km s}^{-1}$ are of the order of the rms spectral noise due to the receiver system and the reduction process. The peak near $+85 \text{ km s}^{-1}$ is due to interference

seems to be accurate, showing a prominent feature without the expanse of negative residuals that would indicate over-correction. Especially striking is the RSL feature in $JD^* = 8324.92$, where the equivalent column density in the reflection profile is no less than $N_{\text{HI}}(\text{RSL}) = 2.84 \cdot 10^{19} \text{ cm}^{-2}$, or 44% of $N_{\text{HI}}(\text{FSL})$.

Figure 25 shows the effect of the RSL correction on the two quite different profiles that were analyzed earlier (see Fig. 22). The observed (uncorrected) profiles are shown again in Fig. 25a. After subtraction of NSL + FSL + RSL (panel (b)), the spectra are in much better agreement than before (cf. Fig. 22a). The individual RSL components are shown in panel (f). Evidently, reflection occurs in spectrum A at the velocity for which the FSL profile reaches

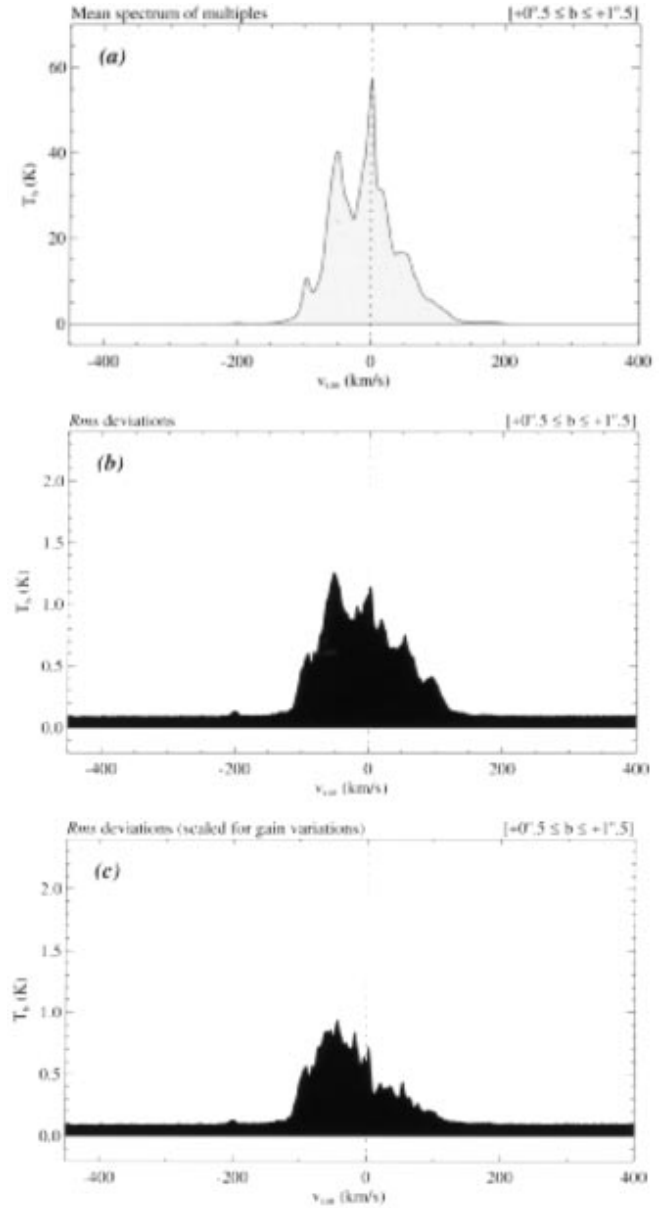


Fig. 30. **a)** Mean of the averaged multiply-observed spectra in the latitude strip $0.5^\circ \leq b \leq 1.5^\circ$. The spectrum has little astrophysical relevance (but it does show the generally high spectral intensities near the galactic plane). **b)** Mean of the channel-by-channel rms deviations of the individual (multiply-observed) spectra from their averaged profiles. The deviations are mostly due to the uncertainties in the calibration of the spectra, which are of the order of 1%. Such deviations propagate in the NSL corrections because the NSL antenna pattern was convolved with the input sky created from these same (uncorrected) data. **c)** After a first-order scaling correction was applied, the deviations are reduced. This scaling correction was calculated from the ratio of the total integrated intensities of the individual spectra towards identical directions. Scaling by this ratio corrects the individual calibration discrepancies, but does not resolve the uncertainties arising from the NSL stray-radiation correction

a maximum, and where the residual component was seen in Fig. 22b. It is still present, since the RSL component appears to have removed only a narrow portion from the center of the feature. The RSL correction in spectrum B was less successful, although still suggestive; the intensity and width of the RSL profile match the left-over component, but the central velocities do not agree.

4.3.6. Results in the LJM Hole data

The results of the stray-radiation and ground-reflection correction applied to the spectra in the test suite of observations toward the LJM Hole are summarized in Table 4. Column densities are given for the observed profiles as well as for the corrected ones. The individual contributions of the various stray-radiation components are expressed as equivalent column densities. We generalize these results below, in an attempt to estimate the accuracy of the stray-radiation correction applied to the entire Leiden/Dwingeloo HI survey.

5. Accuracy and conclusions

5.1. Estimate of the accuracy

The accuracy of the spectra in the survey is generally determined by the precision with which the stray radiation has been determined. In the previous sections we discussed the various manifestations of stray radiation on the HI spectra. We have reduced all profiles entering the survey for the combined NSL + FSL contamination. The reflection correction was calculated for various spectra, but not applied because of uncertainty regarding the parameters which influence this process.

In addition to more information on ground reflection, an improved stray-radiation correction would require more detailed information on the antenna pattern, including knowledge about possible telescope distortions depending on the elevation of the main beam. Furthermore, a more accurate input sky than the coarse ($2^\circ \times 2^\circ$) input sky we used would be required. We note, however, that although such detailed knowledge could, in principle, be obtained, it would exceed the computational resources presently available to us.

The criterion used to estimate the accuracy of the present correction algorithm is based on the assumption that repeated observations towards the same line of sight must yield identical spectra. (It was, after all, such an expectation that first led to the practical recognition of the contaminating properties of stray radiation). Discrepancies between individual profiles and their mean are a measure of accuracy for the entire reduction procedure. We note that such a measure indicates only the relative accuracy; inaccuracies on an absolute scale cannot be determined in this way.

In order to explain the residual spectral component as left-over stray-radiation, we must exclude the possibility that they are spurious instrumental effects rather than emission received in the side lobes. We make the a priori assumption that HI emission from the sky (significantly above the rms noise level) has positive intensities only, except towards lines of sight where there is absorption against strong continuum background sources. We therefore demanded that the correction procedure never yielded negative-intensity intervals in the corrected spectrum. This constraint may have produced spectra in which the true amount of stray radiation was underestimated.

For the 24 spectra in the test suite of observations towards the LJM Hole we calculated the mean spectra and the residuals for three different cases, namely for uncorrected profiles (corresponding to T_a^*), for profiles corrected for NSL and FSL stray radiation (T_b), and for profiles which were additionally corrected for RSL contamination (T_b). From the residual spectra we calculated the channel-by-channel rms deviations from the mean value as an indication of the velocity-dependent accuracy of the intensities in the individual spectra.

Figure 26a shows the mean of the uncorrected spectra in the test suite; Fig. 26b gives the rms values for all the channels. The peak uncertainties are about 0.35 K near $v_{\text{LSR}} = -45 \text{ km s}^{-1}$, while the mean rms uncertainty over the velocity interval $|v_{\text{LSR}}| \leq 100 \text{ km s}^{-1}$ amounts to some 0.16 K.

After applying the NSL + FSL correction, the results are greatly improved, as shown in Fig. 27. The peak and mean rms uncertainties are now 0.16 K and 0.10 K, respectively. The brightness temperature at the velocity of the largest residual is about 0.25 K, compared to 0.7 K in the mean T_a^* profile. The additional correction for ground reflection yields mean rms uncertainties of the order of the spectral noise due to the receiver and the reduction procedure. Figure 28 shows the mean profile in (a), and an practically-flat rms spectrum in (b). We note, however, that the spectra in this test suite were used to optimize the RSL correction algorithm and are therefore not representative of the general accuracy that can be obtained from applying the reflection correction. The results obtained with this additional correction were generally not satisfactorily, although the average correction for the test spectra is quite good. The application of the RSL correction to individual profiles of the test suite yielded mixed results (see Fig. 24).

To estimate the general accuracy of the stray-radiation correction procedure we need an unbiased sample of residual profiles from repeatedly-observed spectra. The scheduling of observations in boxes which overlap at their boundaries (see Hartmann & Burton 1996) was a deliberate choice to ensure repeated observations for many lines of sight. Because the priority of observing the boxes depended on the declination of each central position, the

observations in the directions where multiples would appear were spread out over the entire observing period. We consider the accuracy derived from comparing the residuals from such randomly (time) spaced multiple spectra as being representative for the entire dataset.

We compared multiply-observed spectra in two latitude strips, one at high latitude, the other near the galactic equator. We discuss the results for each of these strips separately.

5.1.1. Multiple spectra at high latitudes

Repeated observations towards identical lines of sight in the latitude strip $+65^\circ \leq b \leq +70^\circ$ observed throughout the entire observing period were used to estimate the accuracy of the FSL stray-radiation correction. At high latitudes the major stray contribution originates from the far-sidelobe region of the antenna pattern. From Table 4 we infer that in directions of low column density approximately equal amounts of radiation are received by the main beam and by the far sidelobes. It is therefore evident that uncertainties in the FSL profile determination will be mainly responsible for the inaccuracies in the corrected spectra.

Table 4. Summary of the properties of the spectra in the test suite of observations towards the LJM Hole. The extreme values, the mean, and the standard deviation (all expressed in equivalent column densities in units of 10^{19} cm^{-2}) of the observed and of the corrected spectra are listed. The contributions from the individual correction components are given separately. On average, a corrected spectrum towards the Hole contained only about $\frac{1}{3}$ of the observed column density. The mean equivalent column densities of the corrections were distributed for 62% over the FSL, for 28% over the NSL, and for 10% over the RSL

component	min	mean	σ_{mean}	max
NSL	2.81	2.82	0.009	2.84
FSL	4.77	6.29	0.86	7.30
RSL	0.23	1.08	0.61	2.84
FSL + RSL	6.24	7.37	0.94	9.35
NSL + FSL + RSL	9.05	10.19	0.94	12.18
observed	12.32	15.33	1.84	18.83
corrected (no RSL)	4.44	6.22	1.25	8.80
corrected (with RSL)	3.27	5.13	1.26	7.95

A total of 456 pairs of repeatedly-observed spectra were averaged, and the rms deviations were calculated. The mean profile of all averaged spectra is shown in Fig. 29a. This profile has little astrophysical relevance (but it does give an indication of the generally low intensities in this latitude strip). Figure 29b shows the channel-by-channel rms deviations, σ , averaged over all multiply-observed spectra. Channels at velocities outside the range over which the stray-radiation correction was

applied ($-250 \leq v_{\text{LSR}} \leq +250 \text{ km s}^{-1}$) are, of course, unaffected and reflect the general accuracy of the reduction procedure. The average uncertainties over the velocity interval $|v_{\text{LSR}}| \leq 100 \text{ km s}^{-1}$, σ_{100} , are about 0.11 K, with a maximum deviation of 0.24 K at $v_{\text{LSR}} = 0 \text{ km s}^{-1}$. We compared the value of σ_{100} with the mean rms deviation for $|v_{\text{LSR}}| \geq 100 \text{ km s}^{-1}$, which we call the *general reduction accuracy*, σ_{red} . For the high-latitude strip we determined $\sigma_{\text{red}} = 0.096 \text{ K}$. We estimated the uncertainties due to the stray-radiation correction, σ_{stray} , by disentangling σ_{red} and σ_{stray} from σ_{100} , yielding $\sigma_{\text{stray}} = 0.052 \text{ K}$. Using the mean rms spectral noise value of 0.07 K determined over the entire survey, the accuracy of the stray-radiation correction procedure as applied to low-intensity spectra was calculated as $\sigma_{\text{stray}} = 0.084 \text{ K}$.

5.1.2. Multiple spectra at low latitudes

We averaged 365 pairs of repeatedly observed spectra in the latitude strip $+0:5 \leq b \leq +1:5$. The mean spectrum of all averaged profiles is shown in Fig. 30a. Again, we note that such a spectrum has little astrophysical relevance (but it does indicate the generally high intensities near the galactic equator). As was seen from Figs. 15 and 16, for example, FSL stray radiation near the galactic plane is insignificant compared with the NSL contribution. Inaccuracies in the stray-radiation correction at low $|b|$ are thus expected to be mainly caused by errors in the NSL component. Figure 30b shows the mean rms uncertainties derived from comparing the pair profiles. Because of the high spectral intensities in these spectra we cannot ignore the general uncertainty in the brightness temperature calibration, which was estimated at about 1%. We corrected the errors introduced by this gain inaccuracy to first order, by scaling the multiple spectra such that their total integrated intensities were equal. The resulting rms uncertainties after this scaling correction was applied are shown in Fig. 30c. We derive a value of $\sigma_{\text{stray}} = 0.51 \text{ K}$ from disentangling σ_{stray} and σ_{red} (0.105 K) from σ_{100} (0.52 K). Without applying the gain-variation correction, the mean net uncertainty, pertaining to spectra of the highest intensities, is $\sigma_{\text{stray}+\text{gain}} = 0.75 \text{ K}$. The inaccuracy in the NSL stray-radiation correction is probably predominantly caused by errors in the input sky. As the input sky was created from the uncorrected survey spectra, the gain fluctuations propagate into the correction profile upon convolving the NSL pattern with the input sky. The coarseness of the sky cells of the input sky, especially in directions where the HI intensity gradients are high, may also contribute to the errors in the NSL profile determination.

5.1.3. Conclusions

The results derived from the test suite of observations towards the LJM Hole, from the high-latitude strip multiples, and from the repeated observations near the

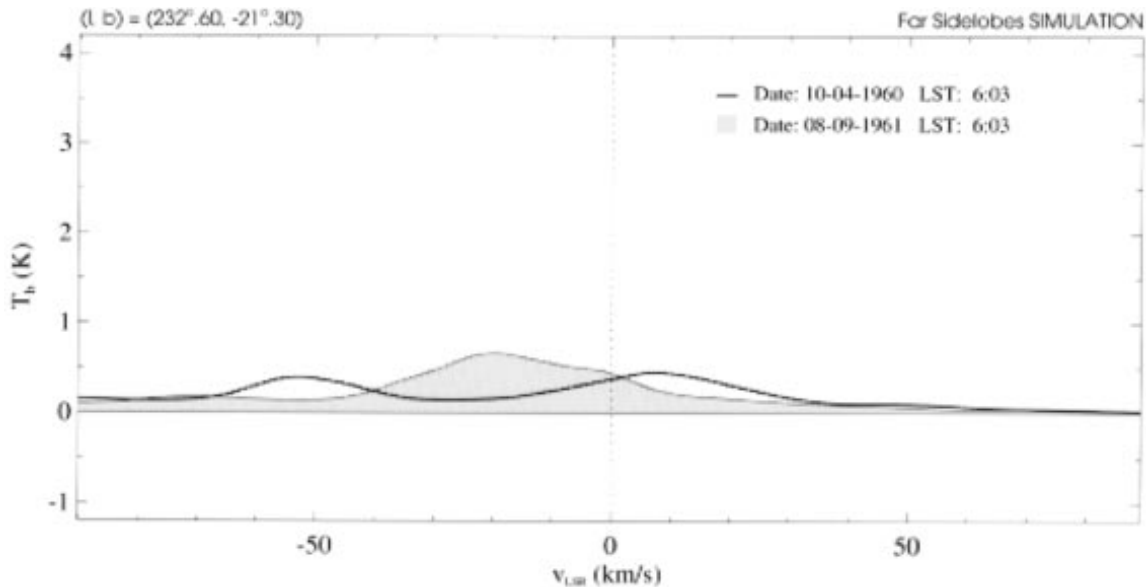


Fig. 31. Simulation of the FSL contaminations in the two spectra published by Van Woerden et al. (1962) made using the model of the current FSL antenna pattern. These stray profiles show that Van Woerden (1962) correctly interpreted the discrepancies seen in Fig. 1 as stray radiation

galactic equator, are summarized in Table 5. The mean rms deviations were determined from the channel-by-channel calculations over three velocity intervals. The values over the effective total velocity range ($-450 \leq v_{\text{LSR}} \leq +400 \text{ km s}^{-1}$) are given, as well as the values for $|v_{\text{LSR}}| \leq 100 \text{ km s}^{-1}$, and $|v_{\text{LSR}}| \geq 100 \text{ km s}^{-1}$.

We are thus led to state the general accuracy of the Leiden/Dwingeloo HI survey as follows. Uncertainties in the stray-radiation corrected spectra due to the FSL correction are less than 0.1 K, and the uncertainties due to the NSL correction are of the order of 2%. The general accuracy of the brightness-temperature calibration of about 1% is responsible for the larger part of the NSL errors.

5.2. Improvements

The accuracy of the stray-radiation correction procedure is limited by three factors.

1. Antenna pattern. We used the averaged NSL response of the WSRT telescope antennas as an approximation of the Dwingeloo NSL antenna pattern. The accuracy of the WSRT pattern cannot compensate for the (slight) dissimilarities between the antennas. Determination of the NSL pattern of the present Dwingeloo antenna by direct measurement of the NSL response may improve the NSL stray-radiation correction, although limitations concerning the accuracy and resolution of the input sky are probably of greater influence. We note that such empirical determination is presently not feasible, as the possibility of creating a two-element interferometer from the 25-m and a reference antenna no longer is an option.

The model for the FSL antenna pattern was derived from the published data of HBDG. We believe that the feed-back procedure employed in tuning the parameters of the model produced an accurate final estimate of the FSL response of the Dwingeloo antenna. An improved determination of the antenna pattern from direct measurements might yield more accurate FSL corrections, but only if the computer implementation of the correction algorithm is calculated to a higher spatial resolution. Again, we note that such an empirical determination is presently not feasible.

2. Input sky. The input sky was created from the uncorrected survey data, binned into $2^\circ \times 2^\circ$ cells. The size of the cells was determined by the spatial resolution employed in the computer implementation of the correction algorithm. The general error of about 1% in the calibration of the brightness-temperature scale propagates directly into the calculated NSL profiles, and increases the uncertainties in the corrected spectra by approximately 2%. Using an input sky created from binning the stray-radiation-corrected survey might yield an improvement in the determination of the stray profiles. For the NSL correction, however, the gain variations will remain the major source of uncertainty.

There is presently no HI dataset available which can improve the correction procedure by using it as an input sky. The saturation effects in the Bell Labs survey for intensities greater than 40 K, and its low velocity resolution of 10 km s^{-1} , make this dataset unsuitable for use with our correction algorithm.

Table 5. Summary of the rms deviations of multiply-observed spectra averaged over three velocity intervals. The results for 24 observations towards the LJM Hole, expressed in equivalent column densities in units of 10^{19} cm^{-2} , are compared for uncorrected profiles (T_a^*) and for stray-radiation-corrected profiles, both with and without a reflection component. A reliable estimate of the mean accuracy for the FSL correction is derived from multiply-observed spectra in a high-latitude strip. Errors in the NSL correction are derived from repeated observations towards directions close to the galactic equator. The results for the NSL rms estimates are corrected for the effects of the general uncertainties in the brightness-temperature calibration. In the text the accuracy of the correction procedure, σ_{stray} , is derived from σ_{100} , and disentangled from the mean errors due to the receiver noise and the reduction procedure, σ_{red}

spectra:	[-450, +400]	[-100, +100]	[-450, -100] & [+100, +450]
LJM Hole T_a	0.098 ± 0.050	0.158 ± 0.073	0.079 ± 0.013
LJM Hole T_b	0.084 ± 0.018	0.100 ± 0.022	0.079 ± 0.013
LJM Hole T_b (with RSL correction)	0.081 ± 0.014	0.090 ± 0.014	0.079 ± 0.013
$65^\circ \leq b \leq 70^\circ$ mult.	0.095 ± 0.020	0.109 ± 0.012	0.096 ± 0.0024
$0^\circ.5 \leq b \leq 1^\circ.5$ mult.	0.260 ± 0.300	0.760 ± 0.240	0.110 ± 0.0047
$0^\circ.5 \leq b \leq 1^\circ.5$ mult. (with scaling correction)	0.203 ± 0.208	0.520 ± 0.220	0.105 ± 0.0032
	σ	σ_{100}	σ_{red}

3. Computer implementation. The computational effort involved in the present implementation of the correction algorithm was considerable. Even though the calculations of both the NSL and the FSL stray profile require merely one CPU second on a DecStation 3000/500 computer, increasing the spatial resolution of the correction would increase the computational burden considerably. (This would only partly be due to the increased number of floating-point calculations, mostly coordinate transformations, that would have to be performed; the efficiency of the calculations strongly depends on whether or not both the resolving kernel and the input sky can remain in core memory between consecutive corrections.)

We suggest that the most practical improvement over our application of the stray-radiation correction would be reached by using the *corrected* HI sky to create an input sky of cell size $1^\circ \times 1^\circ$. Observations should also be performed to obtain more detailed knowledge of the characteristics at 21-cm wavelength of reflection from the ground, under various conditions; this is evidently an important but unfortunately poorly understood phenomenon.

5.3. Van Woerden's estimate

Out of curiosity, we simulated the first detection of HI stray radiation in the observations of Van Woerden et al. (1962). We created two dummy spectra containing approximations of the observing dates of the spectra shown in Fig. 1. Because we suspected that the differences in the spectra were mainly due to seasonal influences, we calculated both corrections at culmination. (Hour-angle dependencies in the original profiles must have disappeared, because the spectra shown by Van Woerden et al. were the averages of many observations.)

Of course, the geometry of the telescope is very different now than it was in 1960–61. The main feature responsible for the stray radiation was the spillover ring, according to Van Woerden (1962), and this probably has not changed much, at least not in its location in the antenna pattern. The FSL calculations for $(l, b) = (232^\circ.60, -21^\circ.30)$ on 10 April, 1960, and on 8 September, 1961, (the averaged dates of the original observations) are shown in Fig. 31. The profiles indicate that Van Woerden correctly interpreted the differences in the spectra as stray radiation. The excess emission near $v_{\text{LSR}} = -50 \text{ km s}^{-1}$ in April, 1960, as well as the September, 1961, emission near $v_{\text{LSR}} = -20 \text{ km s}^{-1}$, are present in the FSL profiles calculated now, some 35 years later.

Acknowledgements. Part of this work was supported by the Netherlands Foundation for Research in Astronomy (NFRA) with financial support from the Netherlands Organization for Scientific Research (NWO). The Dwingeloo 25-m telescope is operated by the NFRA.

References

- Baars J.W.M., 1973, IEEE Trans. Antennas Propagat. 21, 461
Bolton J.G., Stanley G.J., 1948, Aust. J. Sc. Res. A 1, 58
Bracewell R.N., 1956, Aust. J. Phys. 9, 297
Hartmann Dap, 1994, The Leiden/Dwingeloo Survey of Galactic Neutral Hydrogen, Ph.D. Thesis, University of Leiden
Hartmann Dap, Burton W.B., 1996, Atlas of Galactic Neutral Hydrogen. Cambridge University Press (in press)
Hartsuijker A.P., Baars J.W.M., Drenth S., Gelato-Volders L., 1972, IEEE Trans. Antennas Propagat. 20, 166 (HBDG)
Heiles C., Habing H.J., 1974, A&AS 14, 1
Hunt A., Wright A., 1992, MNRAS 258, 217
Jahoda K., Lockman F.J., McCammon D., 1990, ApJ, 354, 184
Kalberla P.M.W., 1978, Die Korrektur der Linienprofile der 21-cm Emission bezüglich der Streustrahlung des Antennendiagramms, Ph.D. Thesis (in German; English translation by R.J. Cohen), University of Bonn

- Kalberla P.M.W., Mebold U., Reich W., 1980, *A&A* 82, 275 (KMR)
- Kraus J.D., 1966, *Radio Astronomy*. McGraw-Hill, New York
- Kuntz K.D., Danly L., 1992, *PASP* 104 (No. 682), 1256
- Lockman F.J., Jahoda K., McCammon D., 1986, *ApJ* 302, 432 (LJM)
- Mentzer J.R., 1955, *Scattering and Diffraction of Radio Waves*. Pergamon, London
- Muller C.A., Westerhout G., 1957, *BAN* 13, 151
- Murphy E.M., 1993, *The Beam Pattern of the 140-Foot Telescope at 1390 MHz*, M.A. Thesis, University of Virginia
- Raimond E., 1964, *Hydrogen Connected with Two Stellar Associations in Monoceros*, Ph.D. Thesis, University of Leiden
- Rohlfs K., 1986, *Tools of Radio Astronomy*. Springer-Verlag, Berlin
- Stark A.A., Gammie C.F., Wilson R.W., et al., 1992, *ApJS* 79, 77
- Staveley-Smith L.S., 1985, Ph.D. Thesis, University of Manchester
- van Someren Greve H., 1991, in *Proc. Workshop "Holography Testing of Large Radio Telescopes"*, Nauka, Leningrad
- van Woerden H., 1962, *De Neutrale Waterstof in Orion*, Ph.D. Thesis (in Dutch), University of Groningen
- van Woerden H., Takakubo K., Braes L.L.E., 1962, *BAN* 16, 321
- Weaver H.F., Williams D.R.W., 1973, *A&AS* 8, 1
- Willacy K., Pedlar A., Berry D., 1993, *MNRAS* 261, 165
- Williams D.R.W., 1973, *A&AS* 8, 505